Seismic Structure of the Upper Crust From 0-75 Ma in the Equatorial Atlantic Ocean on the African Plate Using Ultralong Offset Seismic Data

P. Audhkhasi, S. C. Singh

Geochemistry, Geophysics, Geosystems

AGU100 ADVANCING EARTH AND SPACE SCIENCE

RESEARCH ARTICLE
10.1029/2019GC008577

Seismic Structure of the Upper Crust From 0–75 Ma in the Equatorial Atlantic Ocean on the African Plate Using Ultralong Offset Seismic Data

P. Audhkhasi[1] and S. C. Singh[1,2]

[1]Equipe de Géosciences Marines, Institut de Physique du Globe de Paris (CNRS, Paris Diderot, Sorbonne Paris Cité), Paris, France, [2]Earth Observatory of Singapore, Nanyang Technological University, Singapore

Key Points:
- Layer 2A *P* velocity and the sediment thickness increase rapidly within first 4 Myr
- Rapid sedimentation near the ridge axis controls active hydrothermal circulation and consequently thickness of Layer 2A
- Layer 2A/2B boundary represents lava/dike boundary at the ridge axis and an alteration front within the lava flow away from the ridge axis

Supporting Information:
- Supporting Information S1

Correspondence to:
P. Audhkhasi,
audhkhasi@ipgp.fr

Citation:
Audhkhasi, P., & Singh, S. C. (2019). Seismic structure of the upper crust from 0-75 Ma in the equatorial atlantic ocean on the african plate using ultra-long offset seismic data. *Geochemistry, Geophysics, Geosystems*, *20*, 6140–6162. https://doi.org/10.1029/2019GC008577

Received 15 JUL 2019
Accepted 4 DEC 2019
Accepted article online 5 DEC 2019
Published online 23 DEC 2019

Abstract The uppermost oceanic crust composes of Layers 2A and 2B, and the boundary between them is debated to be a lava/dike transition or a hydrothermal alteration boundary within the lava unit. Here, we present the analyses of ultralong multichannel seismic data along a 1,500 km long profile covering 0–75 Ma of the oceanic lithosphere on the African plate in the equatorial Atlantic Ocean. We find that the Layer 2A is observed along the whole profile, with its *P* velocity increasing from 2.5 km/s near the ridge axis to >4 km/s at ~4 Ma with slight variations thereafter. We also find that the sediment thickness increases rapidly from 0 m at the ridge axis to 170 m at 4 Ma, suggesting that there is a link between the high sedimentation rate and the increase in Layer 2A velocity. These observations indicate that crust younger than 4 Myr may be influenced by active hydrothermal circulation. The observed thickness of Layer 2A decreases from ~850 m near the ridge axis to ~600 m at 15 Ma with no significant changes beyond. We also find an increase in Layer 2B velocity from 5.1 km/s at 4 Myr to 5.5 km/s at 46 Myr, suggesting that passive hydrothermal circulation may extend deeper than Layer 2A/2B boundary. We propose Layer 2A/2B boundary to be a lava/dike transition at the ridge axis and a hydrothermal alteration boundary within the extrusive section away from the ridge axis.

Plain Language Summary The upper oceanic crust is usually divided into an upper Layer 2A and an underlying Layer 2B. Some studies propose the boundary between Layers 2A and 2B as a transition from extrusive lavas to the intrusive dikes, whereas some other studies propose the boundary to be a hydrothermal alteration within the extrusive lavas. Here we have analyzed multichannel seismic data along a 1,500 km long profile covering 0–75 Ma of the oceanic lithosphere on the African plate in the equatorial Atlantic Ocean. We observe the Layer 2A/2B triplication along the whole profile which indicates the presence of a high velocity gradient at the transition of 2A and 2B. To constrain the velocity of the upper crust more accurately, we performed high-resolution traveltime tomography of downward extrapolated data to the seafloor at eight different locations at different ages. We found a rapid increase in sediment cover and *P* velocities in the top of Layer 2A within first 4 Myr with not much changes thereafter. Observed velocities at the 2A/2B boundary indicate that it is a lava/dike transition at the ridge axis and a hydrothermal alteration boundary within the extrusive section away from the ridge axis.

1. Introduction

About 70% of the Earth's crust is formed at the mid-ocean ridges by a combination of magmatic and tectonic processes. The nature of oceanic crust depends on the spreading rate (Purdy et al., 1992) and processes such as hydrothermal circulation. The crust at fast and intermediate spreading centers is dominantly formed by magmatic process, whereas at slow and ultraslow spreading ridges, tectonic processes like faulting could dominate, leading to complex crustal structures. In hydrothermal circulation, the seawater enters the crust, gets heated, and cools the oceanic crust. The water also reacts with host rocks, dissolving minerals that can get precipitated on the way up to the seafloor, filling the pore spaces and hence changing the nature of the crust (Alt et al., 2010). Because of the high temperature near the near ridge axis, the hydrothermal circulation is very robust near the ridge axis and decreases as the crust cools and subsides away from the ridge axis. Sedimentation is another factor controlling hydrothermal circulation and evolution of the crust. As the crust subsides with age, sediments are deposited blanketing the oceanic crust from water due to their low permeabilities.

The oceanic crust can be divided mainly into Layers 2 and 3 with sediments as Layer 1. The upper crust, Layer 2, is mainly formed by extrusive lava flows and dikes, whereas the lower crust, Layer 3, is formed by the cooling and crystallization of magma, forming a gabbroic layer (Detrick et al., 1994; Morgan & Chen, 1993). The earliest studies documenting the existence of the uppermost oceanic crust Layer 2 (Hill, 1957; Raitt, 1963) using seismic refraction data indicated that both the velocity and thickness of this layer vary significantly. The Layer 2 is usually further subdivided into two layers: Layers 2A and 2B. The oceanic magnetic anomalies are attributed to Layer 2A, which mainly consists of pillow lavas (Tivey et al., 1998). This overlies the higher *P* velocity Layer 2B. As the Layer 2A is the uppermost layer of the crust, it gets most affected by the different processes, it is important to determine the variation of Layer 2A with age to understand the evolution of the oceanic crust and lithosphere.

Houtz and Ewing (1976) compiled a data set from sonobouys in the Atlantic and Pacific Oceans and concluded that Layer 2A shows a gradual increase in the *P* wave velocity from 3.3 km/s at ridge crest to 4.5 km/s at 40 Ma, where it appeared to merge with the underlying Layer 2B. They found Layer 2B to has an average velocity of 5.28 ± 0.04 km/s with not much age dependency. Whitmarsh (1978) presented the results of a seismic refraction study at distinct ages ranging from 2–79 Ma and found the absence of a relatively low velocity layer in the top 200 m of the oceanic crust at 46 and 79 Ma. He also found that the velocity gradient in Layer 2 (ranging from 0.85–1.35/s) is similar for all the ages. On the other hand, Schreiber and Fox (1977) and Lewis (1978) found an increase in *P* wave velocity with age, which they attributed to be due to the cementation of cracks. Furthermore, Christensen and Salisbury (1972) noted a decrease in seismic velocity with age of basalts from borehole data, which they explained to be due to increased alteration and low grade metamorphism with increasing age in agreement with the results of Le Pichon et al. (1965) and Raitt (1963). Recent studies based on compilations of ocean bottom hydrophone data (Grevemeyer & Weigel, 1996) suggest that velocities in Layer 2A double within 10 Myr of formation of oceanic crust and do not show significant changes beyond. This compilation was expanded by Carlson (1998) who finds velocities in Layer 2A <3 km/s for young crust aged <1 Myr which increase to 4.4 km/s within 7.5 Myr. He also finds that the velocities in Layer 2A rarely reach those of 2B (~5.2 km/s) and suggests Layer 2A persists beyond 40 Ma as a low velocity layer capping the oceanic crust. Recently, Kardell et al. (2019) have analyzed the evolution of Layer 2A with age in the South Atlantic. Their study shows South Atlantic upper crustal velocity increases to 4.2 km/s at 6 Ma and then gradually increases to 4.9 km/s at 71 Ma. The authors attribute continuous evolution of Layer 2A to low temperature hydrothermal circulation and precipitation. They observed higher heterogeneity in Layer 2A velocities and thickness at slow spreading crust as compared to intermediate spreading crust.

A high velocity gradient at the transition of Layer 2A to 2B gives rise to a triplication in seismic records, the cusp of which when stacked gives an image of Layer 2A. This breakthrough in seismic imaging of Layer 2A from seismic reflection data was proposed by Harding et al. (1993). They found a rapid increase in Layer 2A thickness from 100–200 to 250–600 m within 1–2 km of the rise axis at the fast spreading 9°N East Pacific Rise which was attributed to be associated with the dike subsidence beyond the neo-volcanic zone (Harding et al., 1993; Vera & Diebold, 1994). At the intermediate spreading centers, the thickness of Layer 2A at zero age is greater than that at the fast spreading centers but exhibits higher variability and has been found to be in the range of 250–350 m at Juan de Fuca ridge (Canales et al., 2005) and 350–600 m at the Blanco Transform fault (Christeson et al., 2010). A gradual off axis thickening of Layer 2A ranging from < 40% at the Galapagos spreading center Blacic et al. (2004) to 60–90% at Juan de Fuca ridge (Canales et al., 2005) is observed. A good review of the upper 2 km of the oceanic crust at fast and intermediate spreading centers can be found in Karson (2002) and is not discussed here. At slow spreading centers such as the Mid-Atlantic Ridge (MAR), a 1 km thick Layer 2A has been observed at the Lucky Strike segment (Combier et al., 2015; Seher et al., 2010; Singh et al., 2006) and 0.8–1.3 km thick Layer 2A at the Reykjanes segment (Navin et al., 1998; Peirce et al., 2007). A thicker Layer 2A at slow spreading ridges is explained by a slower spreading rate and hence accumulation of the fresh basalts. Off-axis thinning of Layer 2A at slow spreading centers to 350–600 m is observed (Hussenoeder et al., 2002, which is similar to off-axis thickness of Layer 2A at other spreading centers. Estep et al. (2019) have observed Layer 2A in the South Atlantic in crust aged 0–48 Ma with a mean thickness of 760 ± 290 m.

The boundary between Layers 2A and 2B has been debated to be a lava/dike transition (Christeson et al., 1996; Harding et al., 1993; Toomey et al., 1990) or an alteration boundary within the lava unit (Rohr et al., 1988; Vera et al., 1990) or both (Carlson, 2011; Christeson et al., 2010; Karson & Christeson, 2003).

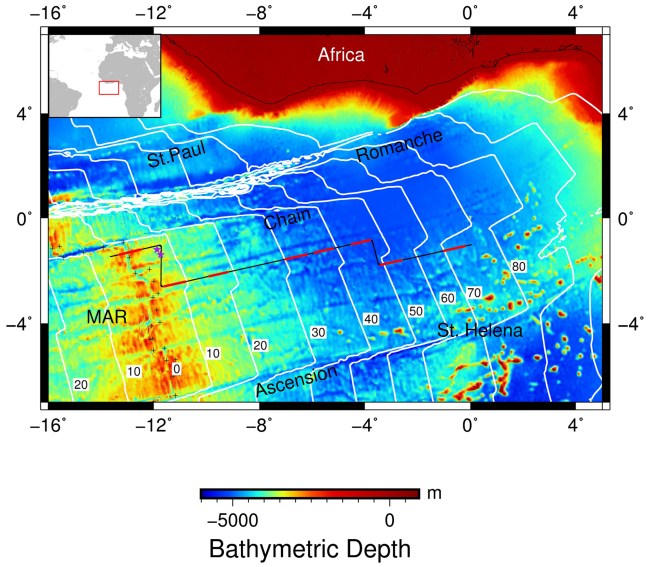

Figure 1. The 15 arc sec global bathymetric map of the study region (Olson et al., 2014) in the equatorial Atlantic showing the multichannel seismic profile in black. The western end of the seismic profile lies at an age of 4.5 Ma on the South American plate, whereas the eastern end of the profile lies near the St. Helena chain at an age of 75.6 Ma on the African plate. The red parts of the profile indicate where downward continuation and tomography have been performed. The Mid-Atlantic Ridge (MAR) from the global plate boundaries map (Bird, 2003) is marked by + signs. Three major fracture zones offset the MAR in the North, St. Paul, Romanche, and Chain, whereas in the south, the Ascension fracture zone offsets the MAR. Between the Chain and the Ascension FZ, the MAR is seen to offset by small distances. The IODP Leg 108 Sites 662 and 663 (Ruddiman & Janecek, 1989) have been marked by purple stars. The age contours have been plotted at every 10 Ma in white from Müller et al. (2008).

From regions where oceanic crust is exposed, the seismic Layer 2A/2B boundary is suggested to be a hydrothermal alteration boundary that can occur at the lava/dike transition such as at Hess Deep or within the lava unit such as at Blanco Fracture zone (Christeson et al., 2007). Borehole studies at Holes 504B and 1256D suggest that hydrothermal alteration at or near the base of lava/dike transition zone is associated with a high velocity gradient leading to the triplication seen in the seismic records (Carlson, 2011). The increase in seismic velocity from Layer 2A to that of Layer 2B has been attributed to a porosity change with depth (Carlson, 2010, 2011, 2014a) or a change in the aspect ratio of the cracks (Wilkens et al., 1991). On the basis of borehole evidence and some seismic studies, Carlson (2018) suggests the dike section to be distinct from Layer 2B and denoted by Layer 2C as observed first by Houtz and Ewing (1976).

Here we present an analysis of ultralong offset (12 km) streamer data to characterize the nature of the upper crust continuously from 0–75 Ma in the equatorial Atlantic Ocean. We first present evidence of Layer 2A from prestack and poststack seismic data followed by high-resolution *P* velocities in the upper 2 km of the crust at distinct ages. This is followed by estimates of porosities from obtained *P* velocities and physical thickness of Layer 2A from seismic two-way time and *P* velocities. We also present sediment cover variations from 0–75 Ma to examine its role in evolution of the oceanic crust.

2. Study Region and Seismic Data Acquisition

The study region lies in the equatorial Atlantic Ocean over the crust formed at the MAR (Figure 1). The present half spreading rate at the MAR is 16 mm/year (DeMets et al., 2010). The origin of the MAR can be traced to ~150 Ma initiated by the continental breakup between the South American and African plates due to the Tristan hot spot. This rifting initiated in the southernmost part of the two continents and led to the formation of the South Atlantic Ocean. At ~110 Ma (Granot & Dyment, 2015), the northward propagating rift reached the equatorial region, where the existence of a colder and stronger lithosphere significantly slowed down the rift and led to the creation of a number of E-W fracture zones (FZs) (Bonatti et al., 1992; Bonatti, 1996). The largest of these is the Romanche FZ having an offset of 900 km and age contrast of 45 Ma. Along with the other two FZs, St. Paul and Chain, the Romanche FZ bounds the northern end of the equatorial segment of the MAR, whereas its southern end is bounded by the Ascension FZ. Our study area lies between the Ascension and Chain fracture zones over the African plate. We have used the seafloor ages from Müller et al. (2008), though some studies obtain different ages (Cogné & Humler, 2004) with the discrepancy being due to the lack of magnetic inclinations in the equatorial region.

In March-April 2015, a 1,764 km long multichannel seismic reflection profile was acquired in this region. A 12 km long IsoMetrix streamer containing multisensors spaced at 3.125 m was used. The multisensors receivers recorded four components: a hydrophone component (*P*), a vertical acceleration component (A_z), and two horizontal acceleration components (A_x and A_y). The streamer was deployed at 30 m depth. The sources consisted of six subarrays, each containing eight air guns, totaling to a volume of 10,170 in.^{3} and were deployed at 15 m. The shot spacing varied from 50–75 m depending on the age of the lithosphere as the objective was to have a higher fold at the younger ages. For older oceanic lithosphere, from 26.7 to 75.6 Ma, the shot spacing was 75 m. For a younger lithosphere of 1.8 to 26.7 Ma, the shot spacing was reduced to 50 m, whereas near the ridge axis, it was increased to 62.5 m. Although the objective was to shoot a 2-D straight profile, it was necessary to shift the profile twice in order to avoid entering into the extended/claimed 560 kilometres (km) exclusive economic zone of Ghana and the United Kingdom. As a result, three legs of ridge perpendicular profiles were acquired. The leg crossing the ridge axis spans an age of 4.5 Ma on the South American plate and 7.7 Ma on the African plate (Figure 1). The largest ridge perpendicular part of the profile spans an age of 1.8 Ma on the African plate near the ridge axis to 46.7 Ma. The southernmost leg

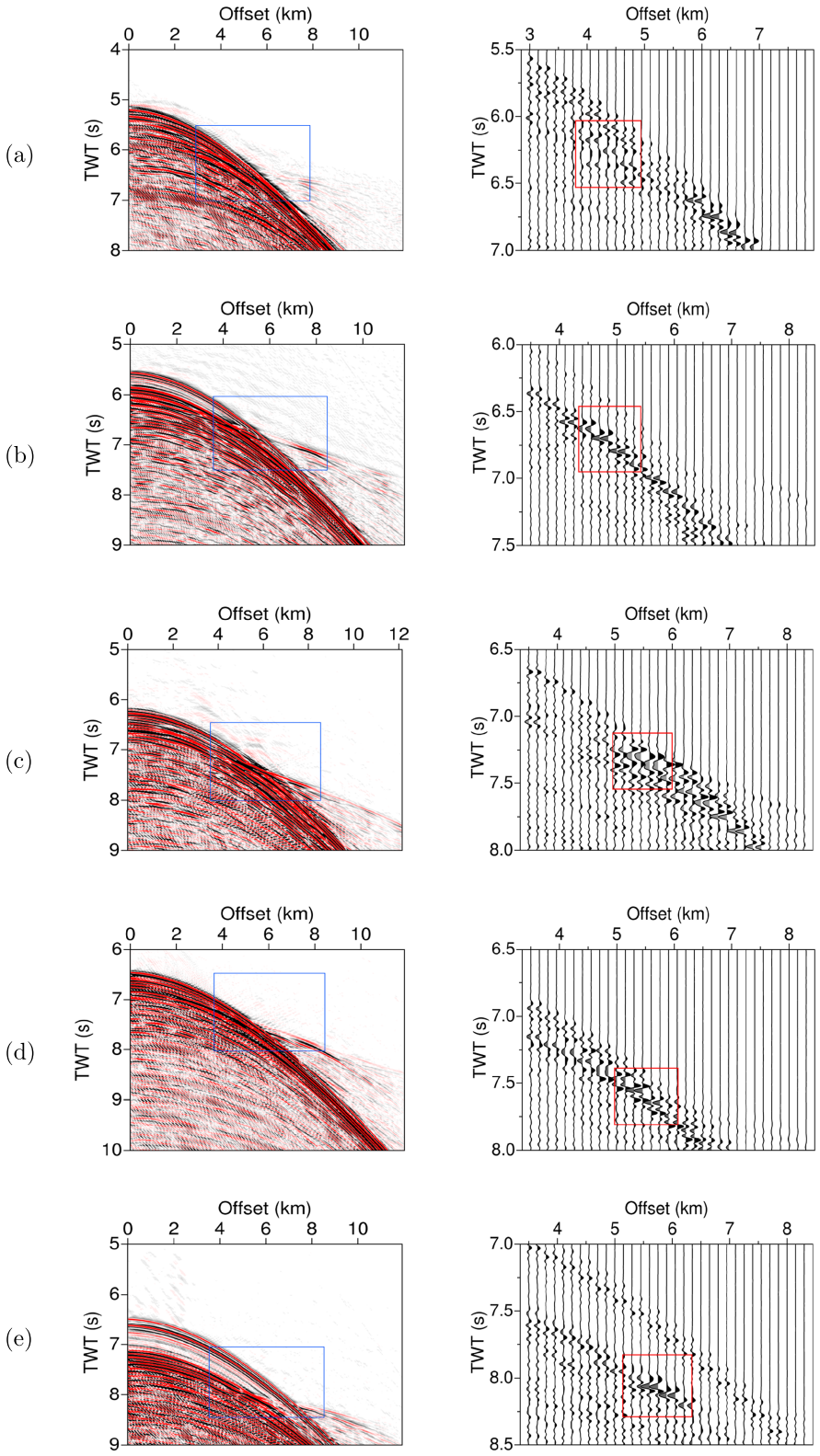

Figure 2. The left panel consists of dip-filtered super-CMP gathers showing Layer 2A triplication at different crustal ages: (a) the median valley of the ridge axis (zero age), (b) 16 Ma, (c) 31 Ma, (d) 50 Ma, and (e) 70 Ma. A shift in triplication can be observed toward the farther offsets as the age increases. The blue rectangled region has been expanded to highlight the triplication in the right panel (rectangled in red). The amplitudes in the right panels are much reduced as compared to left panels.

of the profile spans an age of 49.3 to 75.6 Ma with the St. Helena seamounts further east. The parts of the flow line crossing the ridge axis corresponding to 0 to 1.8 Ma, the largest leg of the flow line corresponding to 1.8 to 46.7 Ma, and the last leg of the flow line corresponding to 49.3 to 75.6 Ma were combined together to create a continuous age variation from 0 to 75.6 Ma. As there are no large offset fracture zones between the Ascension and Chain fracture zones and the MAR segmented on a small scale, the oceanic lithosphere was sampled continuously.

3. Seismic Data and Image of Layer 2A

The pressure and vertical component data were combined to remove the sea-surface ghost and create a broadband seismic response at every 3.125 m using WesternGeco propriety software (Vassallo et al., 2013). These data were then grouped to achieve a trace spacing of 12.5 m after the application of an antialiasing filter. The left panel of Figure 2 shows supercommon-midpoint (CMP) gathers at five different locations, at the median valley of the ridge axis (0 Ma), at ~16 Ma, ~31 Ma, ~50 Ma, and ~70 Ma. The super-CMP gathers were obtained by combing eight neighboring CMP gathers and dip filtered to remove the noise. A close examination of these data indicates the presence of triplications associated with the high velocity gradient at the base of Layer 2A right panel of Figure 2. As one progresses toward mature oceanic crust, the effect of a thicker water column and a sediment cover move the triplication to farther offsets. At zero age, in Figure 2a, the triplication is seen to be at 4–4.5 km offsets and 5.5–6 km at 70 Ma (Figure 2e). The shifting of the triplications to farther offsets could be due to (a) a lower gradient at base of Layer 2A and/or (b) increased thickness of the water column and sediment layer or (c) due to both effects. Figure S1 in the supporting information shows the super-CMP gathers close to the ridge axis.

Seismic reflection data were processed (Figure S2) to obtain the seismic image of Layer 2A (Figure 3). A Normal Moveout (NMO) correction was applied using a constant stacking velocity to best flatten Layer 2A triplication. It should be stated here that the Layer 2A triplication is not a true reflection and the stacking velocity is chosen to get the best image. A constant velocity was chosen instead of separate velocities for seafloor and Layer 2A event in order to avoid the NMO stretch, which would most affect the wide-angle energy specially in a complex seafloor environment. The best stacking velocity for the Layer 2A event was determined from a suite of NMO-corrected super-CMP gathers as well as constant velocity stacks up to an offset range at which the triplications are observed. An uncertainty estimation was carried out to examine the effect of stacking velocities on the two-way travel time (TWTT) of the imaged Layer 2A event (Figure S3). At the ridge axis, a rugged bathymetry results in more variable stacking velocities to flatten the Layer 2A/2B event. The velocities between 1,700 and 1,900 m/s provide the best image. The uncertainty in the Layer 2A thickness is ±70 ms at the ridge axis but is only ±30 ms at 70 Ma due to a thick sediment cover and a flatter basement morphology. The overcorrected arrivals from Layer 2B have been appropriately muted. An additional inner mute for removing the energy prior to the Layer 2A event is also applied before stacking. The imaging is usually better in regions of flatter basement morphology. Poststack processing includes a 0-1-35-40 Hz band-pass filter, constant velocity time migration with water velocity and seafloor mute. Figure 3 shows the five stacked seismic images for different ages.

At the ridge axis, the median valley is observed at 5.2 s TWTT with a clear reflection of Layer 2A at ~500 ms TWTT below the seafloor (Figure 3a). Due to the rugged bathymetry, the Layer 2A is intermittently imaged beneath the ridge flanks at ~550 ms below the seafloor. The uncertainty in the Layer 2A thickness is ±70 ms. No sediment cover is observed at the ridge axis. Figure 3b shows the seismic image at 15.6–17.8 Ma with a rugged basement topography covered with up to 450 ms TWTT thick sediments. A strong amplitude Layer 2A/2B event is imaged at 300 ± 70 ms TWTT below the basement almost throughout the profile with the thinnest in the valley at 52 km. Figure 3c shows the seismic image at 30.4–33.4 Ma having a rugged basement topography and a veneer of thin (100–150 ms) sediment covering the basement. The imaging of the Layer 2A event is best in the western part of the profile. The Layer 2A event is also imaged beyond 25 km distance with weaker amplitudes and where the basement is relatively flat. The seismic TWTT thickness of the Layer 2A varies between 320 and 370 ms TWTT. However, toward the eastern end of the profile, the imaging of the Layer 2A event is poor. The profile at 49.9–52.2 Ma has basement morphology similar to that at 30 Ma and has a thin layer of sediment (Figure 3d). There are three prominent basement valleys—at 15, 40, and 57 km on the profile with sediment thickness varying between 300 and 200 ms TWTT. The Layer 2A event can be observed (300 ms TWTT below the basement) throughout the profile with varying amplitudes. Figure 3e shows the seismic section at 68.6–71.9 Ma, which is at the eastern end of the profile, having an average of

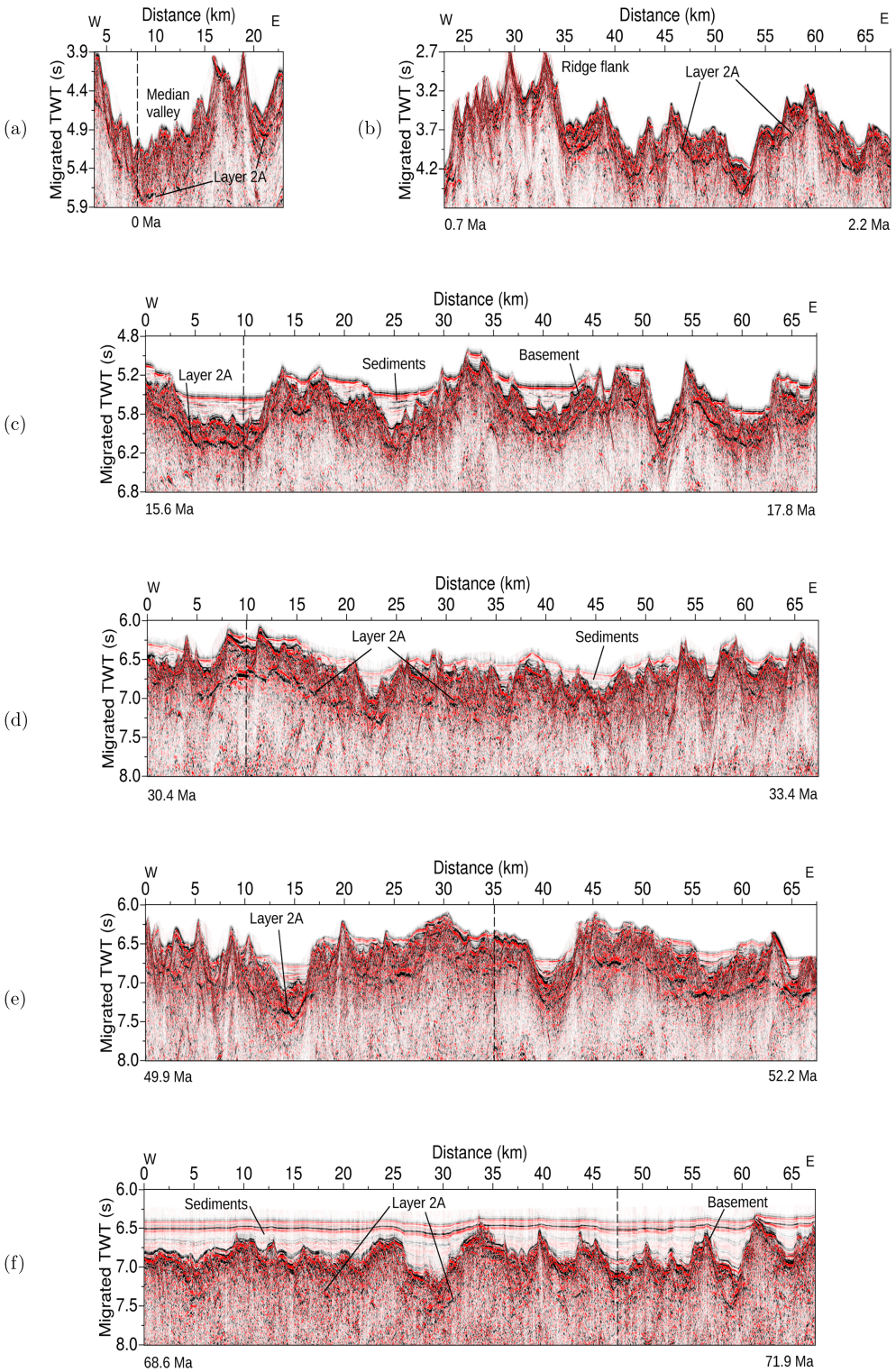

Figure 3. Poststack seismic sections showing the Layer 2A event at different crustal ages: (a) median valley of the ridge axis, (b) 0.7 to 2.2 Ma, (c) 15.6 to 17.8 Ma, (d) 30.4 to 33.4 Ma, (e) 49.9 to 52.2 Ma, and (f) 68.6 to 71.9 Ma. The black dashed line shows the location of the super-CMP gathers in Figure 2.

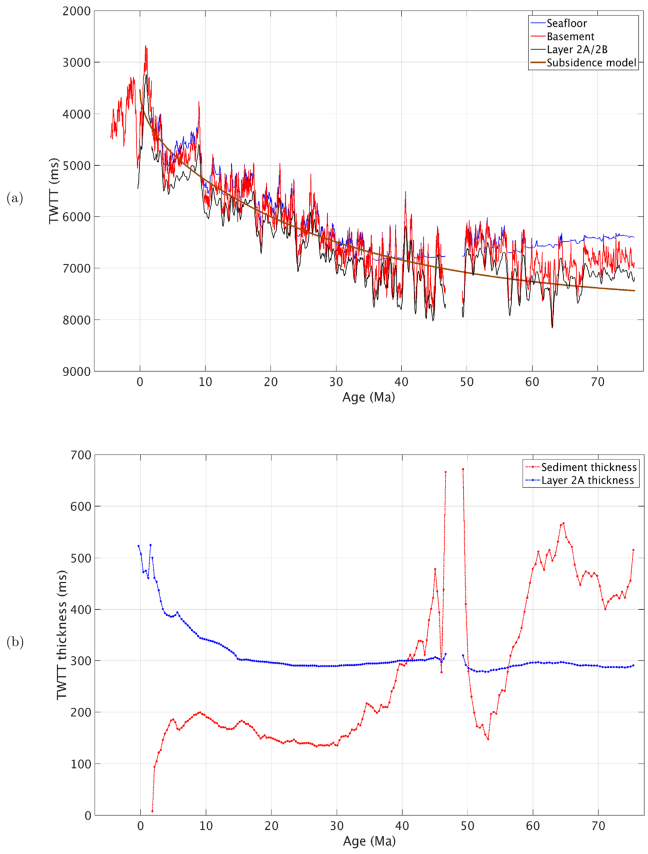

Figure 4. (a) Age versus two-way traveltime (TWTT) plots for seafloor, basement, and Layer 2A/2B interfaces across the ridge-perpendicular segments of the profile. Layer 2A/2B interface refers to Layer 2A/2B boundary. The ridge axis corresponds to zero age. The subsidence of the oceanic crust can be observed as one moves away from the ridge axis. The theoretical subsidence model has been plotted on the basis of Hasterok (2013). Onset of a thicker sediment cover can be seen at 35 Ma on the African plate. An uplifted basement can be seen at 75 Ma which is near the St. Helena seamounts. (b) A smoothed version of sediment thickness and Layer 2A thickness computed from (a). A gradual increase in sediment cover thickness can be observed as one moves away from the ridge axis with the maximum thickness being ~500 ms TWT at 65 Ma. The Layer 2A TWTT thickness rapidly decreases from 500 ms at zero age to 350 ms at 10 Ma and reaches a minimum of 280 ms at ~25 Ma. The seismic TWT thickness of Layer 2A derived from the stack sections has an uncertainty of ±30 ms where the basement is relatively flat and ±70 ms where the basement is rugged (Figure S3).

~500 ms TWTT thick sediment cover, with a maximum of 700 ms at the central basement valley from 27–32 km on the profile. The Layer 2A event is weak, less continuous, and lies roughly ~300 ± 30 ms below the basement.

The TWTT picks for the seafloor, basement, and Layer 2A event from the whole seismic profile covering 0–75 Ma is shown in Figure 4a. The basement topography contains a number of short wavelength features, which are typical at a slow spreading ridge. The seafloor and basement follow each other from 0 to 36 Myr. From 36 to 75 Myr, the seafloor flattens and rises toward the older lithosphere, which could be due to the thickening of the sediments near the African margin. However, there are large topographic features between 40 and 56 Myr, not covered by the sediments, which could be due to the presence of the St. Helena chain. Furthermore, there is also a slight decrease in the average basement depth between 56 and 75 Myr, possibly due to mantle upwelling and higher thermal anomaly associated with the St. Helena chain. A close analysis of the seafloor bathymetry and basement topography indicates that this change starts around 36 Myr, coincidental with the increase in sediment thickness, suggesting that the mantle thermal anomaly may extend up to this distance. The other prominent anomalous feature we observe is a reversed bathymetric slope between 4.5 and 10 Myr.

We have also plotted the age-dependent subsidence curve (Hasterok, 2013) as shown in Figure 4a, which was adjusted for heat flow measurements on older oceanic crust (>80 Ma) (Hasterok et al., 2011). The ridge

axis depth is obtained by least squares fitting of the subsidence model to the basement depth between 0 and 46.7 Myr and is equal to 2,655 ± 20 m. The average upliftment of the basement between 49.3 and 75.6 Myr is 370 ± 20 m relative to the subsidence model. Although the subsidence curve captures the overall trend of the seafloor, there are some anomalies. Between 30 and 46.7 Myr, the average seafloor and basement is slightly deeper than the subsidence model prediction, whereas it is shallower than the predicted model between 49.3 and 75.6 Myr, which further supports the idea that there is an influence of the St. Helena seamounts along half of our profile. The basement topography contains a number of short wavelength features, which are typical at a slow spreading ridge. No sediment cover is observed at the ridge axis.

Figure 4b shows a smoothed version of the Layer 2A and sediment TWT thickness for the whole profile. The sediment thickness linearly increases with age until 4 Myr, with a peak at 9 Myr (200 ms), and decreases to ~140 ms during the next 20 Myr. From 30 Myr onward, a linear increase is observed with the maximum sediment thickness reaching to ~470 ms TWTT at 45 Ma. An anomalous increase in the sediment thickness around 49 Myr is due to the large distance from the Congo river along this segment of the profile. The mean sediment thickness at the end of the profile is 450–500 ms TWTT.

A decrease in the TWTT thickness of seismic Layer 2A is seen with increasing age. At the ridge axis, an ~500 ms TWTT thick seismic Layer 2A is observed. The Layer 2A thickness decreases rapidly to ~350 ms up to ~10 Myr and then linearly decreases to 300 ms at 15 Myr and reaches to a minimum of 280 ms TWTT at 25 Myr. A slight increase is observed beyond 25 Myr until 45 Myr, which then remains constant up to the end of the profile at about 300 ms. Interestingly, a strong correlation is observed in the increase of sediment cover and decrease in Layer 2A thickness within the first 4 Myr.

4. Downward Extrapolation and Traveltime Tomography

The root mean square velocities obtained from the NMO analyses are adequate to image Layer 2A but are not accurate enough to depth convert these images, especially as the NMO velocity is derived not for a continuous reflection event but for a limited offset wide-angle triplication. To estimate the velocity accurately, we performed downward continuation followed by traveltime tomography at eight distinct ages throughout the profile: 0–2.2, 3.1–6.3, 15.6–17.8, 30.4–33.4, 35.1–38.9, 43.7–46, 49.9–52.2, and 68.6–71.9 Ma (Figure 1), but here we will only show results from five locations.

Figure 2 clearly shows that triplications from the high velocity gradient layer at the base of Layer 2A are present at all ages, but they are obscured by the seafloor reflections and therefore are difficult to pick, whereas the far offset first arrivals are from Layer 2B. In order to unfold the triplications in shot-receiver gathers and bring them as first arrivals, a downward extrapolation of the wavefield was performed down to 100–300 m above the seafloor to create a Synthetic On-Bottom Experiment (Arnulf et al., 2011) geometry as if both sources and receivers are just above the seafloor. We tried to keep the datum for downward continuation as close to the seafloor as possible while avoiding surface waves and ensuring that the raypaths between the original datum and the new datum are completely within water. Figure S4a shows the raypaths in water for Pass 1 of downward continuation in which the sources were brought down to the datum. An erroneous datum with raypaths not passing through seawater may map into the tomography models as artifacts. Usually, the energy at zero offset of the shot gathers is lost due to tapering in the downward continuation process. To preserve that energy, the original shot gathers were modified by extrapolating toward negative offsets as shown in Figure S4b. The energy at zero offset is necessary to preserve the first arrivals close to zero offset. A water velocity of 1,496 m/s and a Kirchhoff integration scheme were used to perform the wavefield extrapolation (Berryhill, 1984). Figure 5 shows the corresponding downward extrapolated super-CMP gathers of Figure 2 at distinct ages. The downward extrapolated gathers have larger offset ranges for the first arrivals due to better ray coverage in the upper oceanic crust, hence should provide a better resolution of the upper oceanic crustal velocities. The first arrivals were picked to perform traveltime tomography (Van Avendonk et al., 2004). The offset range for picking varied between 1–2 and 8–10 km.

A 1-D velocity model was hung from the basement to create a 2-D starting velocity model for tomography. The 1-D velocity model for 30, 50, and 70 Ma old oceanic crust was taken from White et al. (1992), whereas for younger crust, the velocity model was taken from Dunn et al. (2005). Velocity analysis for the sediments was carried out at several super-CMP gathers over regions having a relatively flat seafloor and basement. A Dix inversion of these RMS velocities yielded interval velocities of the sediments between 1.62 and 1.85 km/s at distinct ages. For each age, a constant value of the sediment velocity was taken as the mean of all the

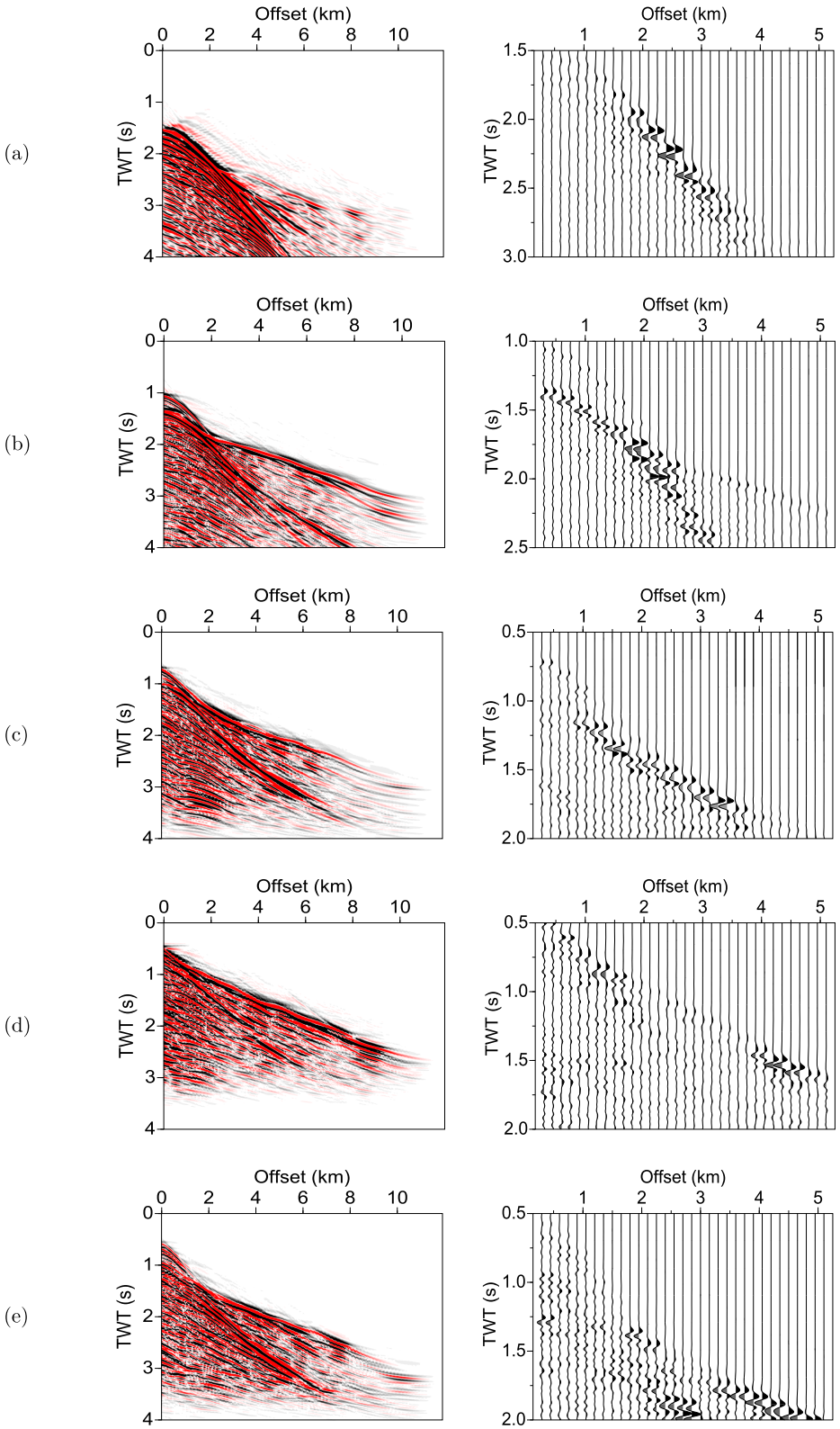

Figure 5. Downward continued super-CMP gathers corresponding to super-CMP gathers of Figure 2 at different crustal ages: (a) the median valley of the ridge axis (zero age), (b) 16 Ma, (c) 31 Ma, (d) 50 Ma, and (e) 70 Ma. The first arrival is much enhanced now as there is better ray coverage through the uppermost oceanic crust. The first 5 km offset of the left panels have been expanded in the right panels.

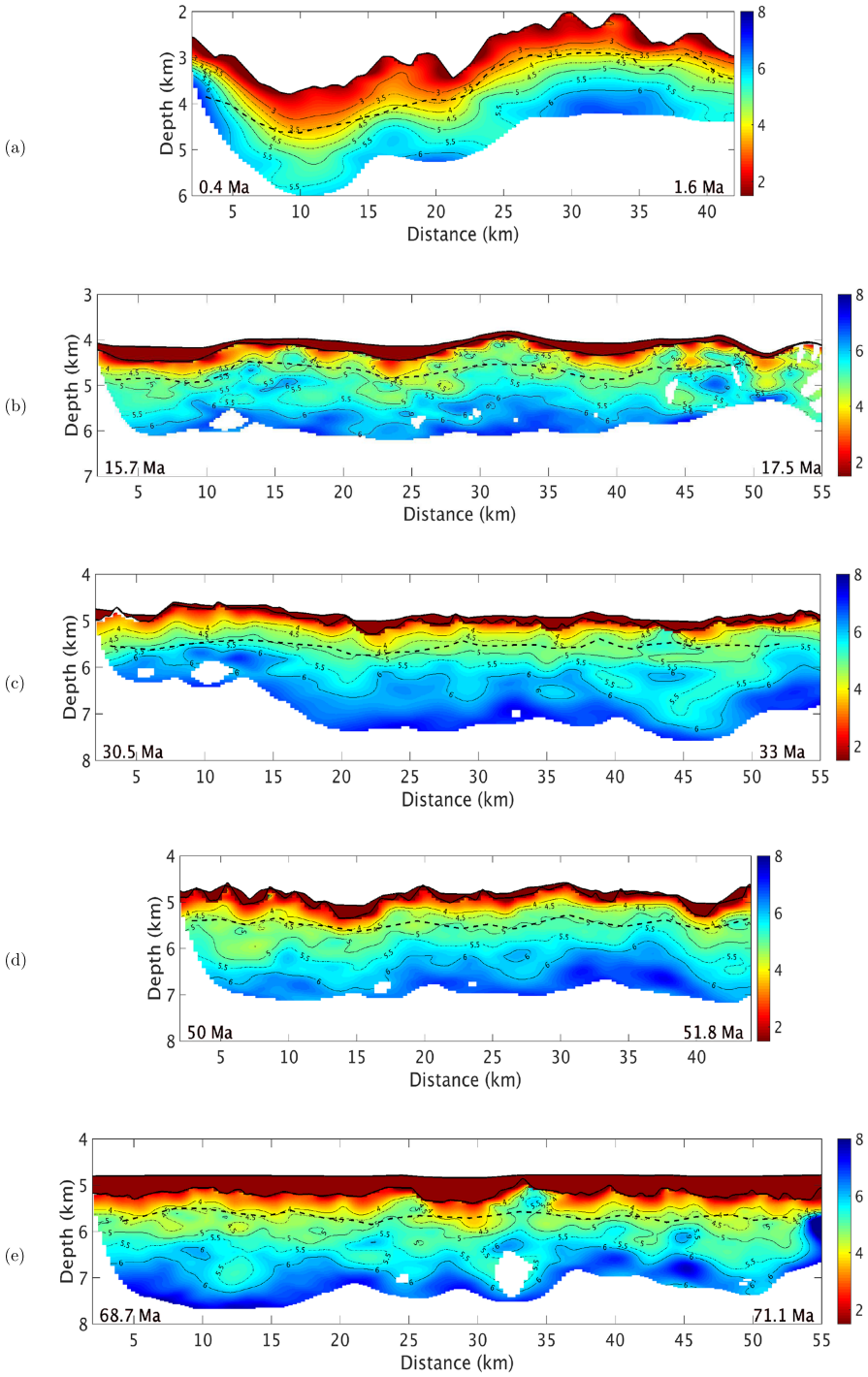

Figure 6. Tomography inversion results at four distinct ages corresponding to sections of Figure 3. The interface corresponds to a smoothed version of the seafloor and basement. The black dashed line corresponds to depth converted smoothed Layer 2A/2B boundary from the seismic using tomography velocities. Regions without any ray coverage have been masked. Sediment velocities have been estimated using RMS velocity analysis from seismic and are listed in Table S5. The distances are plotted with respect to the seismic sections in Figure 3.

computed interval velocities (Table S5). The ray tracing was then performed on the starting model using the shortest path method (Moser et al., 1992), and the inversion used an LSQR algorithm (Van Avendonk et al., 2004). Shots were picked at every 125 m near the ridge axis and at every 150 m elsewhere. The final picking uncertainty is set between 10 and 20 ms, depending on the roughness of seafloor, shot-receiver position uncertainty, and downward extrapolation uncertainty.

Optimum regularization parameters for the inversion was obtained by taking the point of maximum curvature in the L-curve (Hansen & O'Leary, 1993). The regularization parameter was then decreased with every iteration until χ^2 came close to 1, after which they were removed. Only the zeroth-order derivative smoothing and second-order derivative smoothing were used. Several runs of inversion were performed with the starting model of a particular inversion run obtained by averaging the result of the previous inversion run. Each inversion run was ensured to converge to a minimum misfit. This was carried out until the results of two consecutive inversions were same. The graph grid spacing for ray tracing is 12.5 m in both vertical and lateral directions, which is the same as the receiver spacing. The inversion grid spacing was kept at 300 m in the horizontal direction and 50 m in the vertical direction. A further decrease in the inversion grid spacing yielded no better results. A higher regularization was applied in the horizontal direction as compared to vertical direction in all the iterations for obtaining a laterally smooth model, which would facilitate the depth conversion of the Layer 2A/2B from the seismic. The starting interfaces for tomography were the smoothed seafloor and the basement using a moving average window of 300 m, which is the same as the lateral inversion grid spacing. In the regions at 0.5–2.2 and 15.6–17.8 Ma, a higher smoothing (600 m moving average) of the seafloor and/or basement had to be performed to ensure good ray coverage and suppress tomography artifacts.

The final tomography models at different ages are shown in Figure 6. A smoothed version of the Layer 2A/2B boundary has been depth converted from the seismic (Figure 3) using the 2-D tomography *P* velocities from Figure 6 and is overlain on the models. We also show the ray coverage diagrams in Figure S6 and the residuals reduction plot in Figure S7 to further validate our tomography results. The tomography results have been shown in the well-resolved regions, which correspond to regions having sufficiently high ray coverage. The ray coverage diagrams are obtained by the derivative weight sum parameter, which is the sum along all columns of the Fretchet matrix of first derivatives (Van Avendonk et al., 2004). Vertical gradients of velocity models at distinct locations at each age have also been plotted to compare with the depth converted Layer 2A as shown in Figure S8 to further examine their relationship, which will be discussed later.

In order to assess the resolution of tomography, checkerboard tests were performed for different anomaly sizes as shown in Figures 7 and S9. Four different Gaussian anomaly sizes, 2 km × 2 km, 1.5 km × 1.5 km, 1 km × 1 km, and 0.5 km × 0.5 km, with 5% velocity perturbation were tested. The tests were performed at the ridge axis (Figure 7) and at 68.6–71.9 Ma where a thick sediment cover is observed (Figure S9). The checkerboard tests for resolution in both cases yield a limit of 0.5 km anomalies with 5% velocity perturbation.

5. Combined Interpretation of Seismic TWTT and *P* Velocity

The seismic sections in Figure 3 show high-resolution images of Layer 2A in time, whereas the tomography results in Figure 6 show high-resolution *P* velocity models as function of depth for each age window. In order to interpret these two images, we picked the Layer 2A/2B on reflection image and depth converted using tomographic velocities.

At the ridge axis, the seafloor in the median valley has a velocity of ~2.5 km/s (Figure 6a), and the seafloor at the adjacent ridge flanks have a slightly higher velocity reaching ~2.7 km/s. Figure S8a shows 1-D velocities and vertical velocity gradients as a function of depth extracted at distinct locations from Figure 6a. The low gradient part of Layer 2A is not clearly distinguishable from the high gradient part of Layer 2A which could be due to smoothing effects in tomography. The base of the high gradient region lies at 820 ± 315 m beneath the median valley (Figure S8a) and matches well with the reflection image at 500 ms (Figure 3a). The Layer 2A/2B boundary at the median valley does not represent a sharp transition from high gradient region to low gradient region which may be due to reduced gradients and/or smoothing effect in tomography. At the ridge flanks, from 27–32 km distance range, the Layer 2A seismic reflection at 550 ms maps to 900 ± 315 m depth. However, at distances of 21.5 and 36 km, the Layer 2A/2B boundary matches well with the high gradient at base of Layer 2A to low gradient in Layer 2B transition. The change in the vertical velocity gradient takes

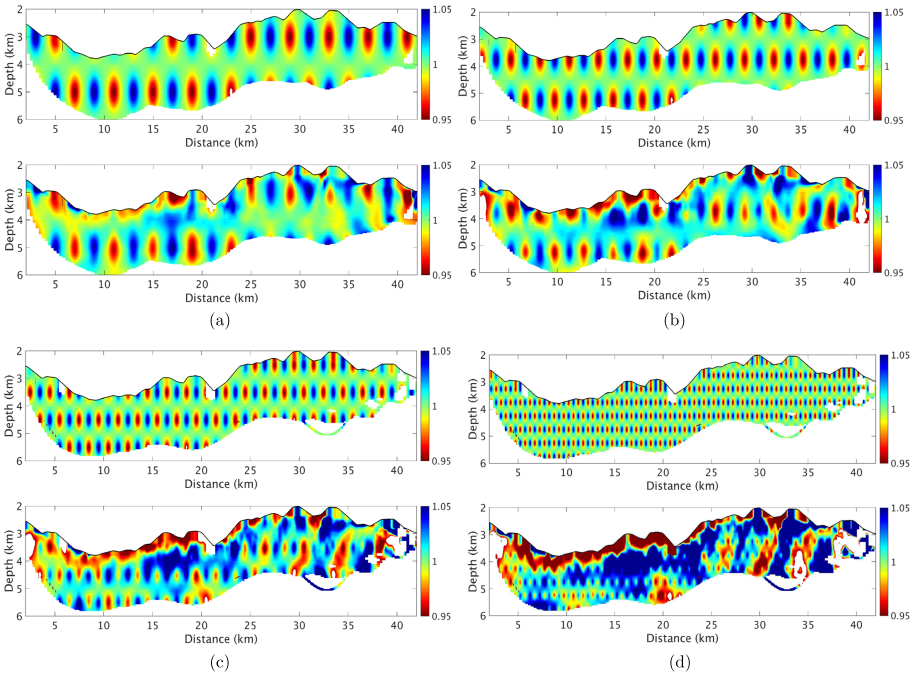

Figure 7. Checkerboard test for resolution at the ridge axis: (a) Top panel shows the 2 km × 2 km checkerboard pattern and below is the recovered; (b) 1.5 km × 1.5 km pattern and the recovered (below); (c) 1 km × 1 km pattern and the recovered (below); and (d) 0.5 km × 0.5 km pattern and the recovered (below). All anomalies are 5% velocity perturbations. The limiting resolution from this test is the dimension of 0.5–1 km of an anomaly having 5%.

place from >5/s at top of Layer 2A to <2/s at the Layer 2A/2B boundary. A reduction of residuals from >1s to a mean of 23 ms is observed in Figure S7a.

An increasing sediment *P* velocity with age can be seen from Table S5. At ages 15.6–17.8, 49.9–52.2, and 68.6–71.9 Ma in Figures S8b, S8d, and S8e, a low gradient 2A can be distinguished from a high gradient 2A, whereas at 30.4–33.4 Ma in Figure S8c, the distinction is not so clear. At almost all ages, the Layer 2A/2B boundary matches well with the transition from high gradient region at the base of Layer 2A (>5/s) to low gradient in Layer 2B (<2/s). This transition is observed at depths of 580–650 m with an uncertainty ranging from ±365 to ±165 m. In regions of thick sediment cover, a better penetration of rays is achieved as shown in Figure S6e due to reduced scattering from the rough basement. Along with the better penetration of rays, the velocities just below the basement are slightly reduced such that velocities at the turning point of the rays remain similar in both thick sedimented and thin sedimented regions. Isolated basement outcrops have velocities close to 5 km/s (Figure 6). Figure S7 shows a good reduction of residuals at all ages.

In order to further validate our tomography models, elastic finite difference synthetic seismograms were generated and compared with the real shot gathers (Shipp & Singh, 2002). The ratio of *P* and *S* velocities was approximated as 1.73 assuming a Poisson's ratio of 0.25 (Collier & Singh, 1998). The velocity model was discretized into a 12.5 m grid, and a Ricker wavelet of 10 Hz dominant frequency was used for generating the synthetic seismogram. This was performed for both downward continued (Figure 8) and surface data (Figure S10) at distinct ages. The left panel of Figure 8 shows plots of the synthetic downward continued shot gathers, and the right panels show the real downward continued shot gathers at the same location. Good match of the first arrival between synthetic and real data is observed at all ages. In almost all the ages, a distinct linear moveout arrival is seen appearing after the first arrival (*P* wave) in the real shot gathers and may correspond to the *S* wave.

The *P* velocities from the tomography were averaged at every ~1 Myr(~10 km) at all distinct ages to get the global age variation as shown in Figure 9. The tomography results cover >24 Myr of the 75 Myr of the profile. For getting the best estimate of Layer 2A velocities, velocities were picked at a depth below the basement which corresponded to the turning point of the ray emerging at the first picked offset used in tomography. This corresponds to ~200 m below the basement for the first picked offset being ~1 km.

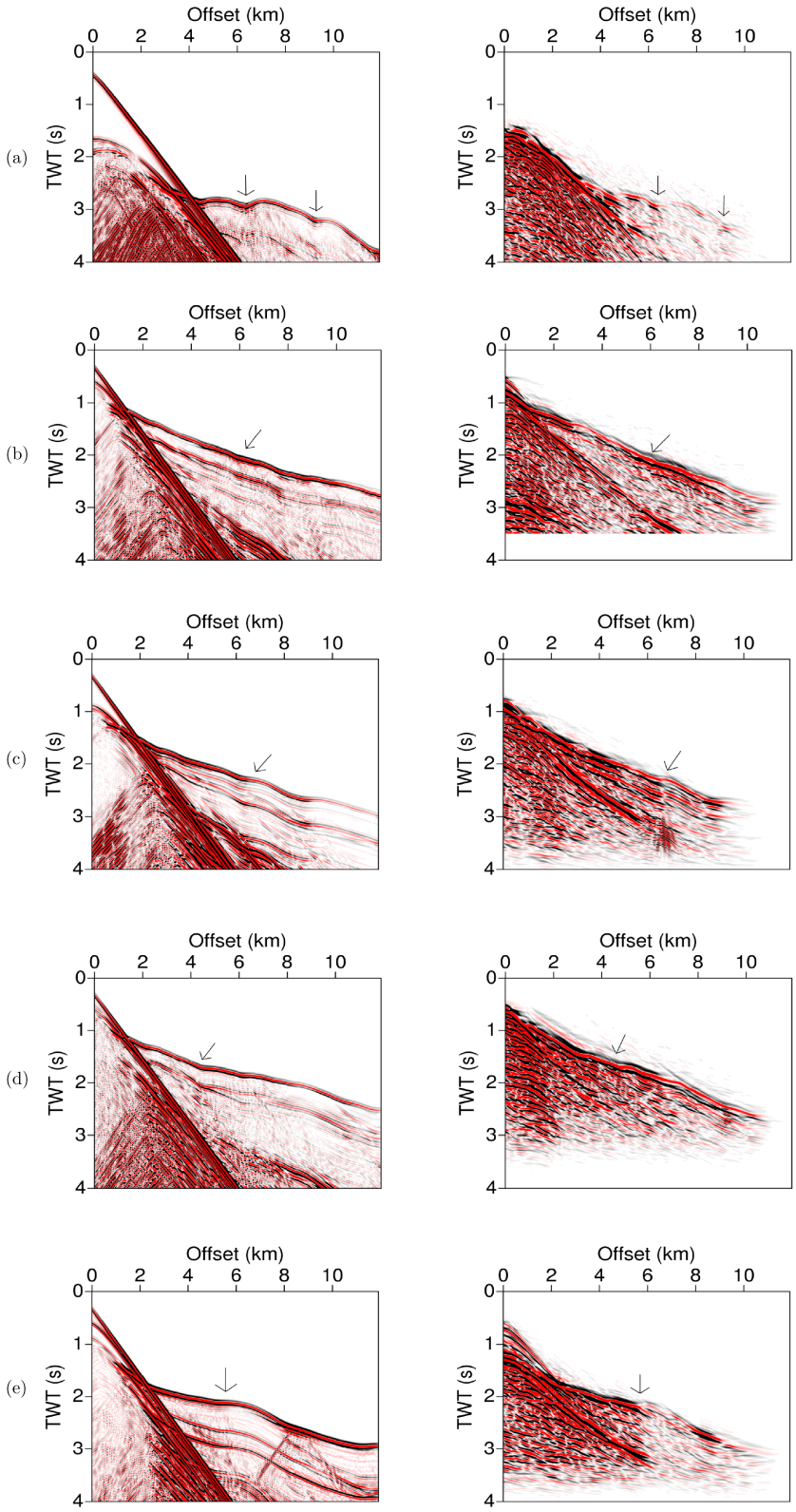

Figure 8. Final synthetic and real shots gathers for downward continued data at distinct ages. A Ricker source wavelet of dominant frequency of 10 Hz has been used for elastic modeling of the synthetic shot gathers (Shipp & Singh, 2002). A good match can be found between the first *P* arrival of the synthetic and real gathers as indicated by the arrows indicating a good reliability of tomography models. V_p/V_s ratio has been taken to be 1.73 from Collier and Singh (1998).

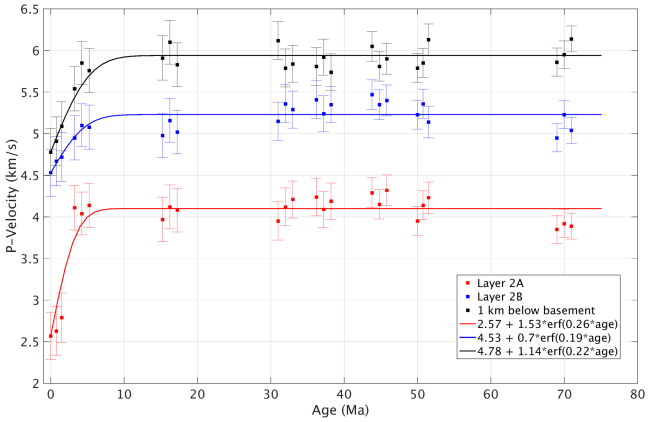

Figure 9. *P* velocities of Layer 2A (red), Layer 2B (blue), and at 1 km below the basement (black) plotted as a function of age. At each region where tomography has been performed (Figure 6), velocities were averaged for Layer 2A ~200 m below the basement and along the Layer 2A/2B boundary for Layer 2B at every 1 Ma. The uncertainties in the velocities are denoted by the error bars. The best fitting curves for the *P* velocities are modified equations from Grevemeyer and Weigel (1996) and are shown by solid lines. The velocities become statistically constant beyond 4 Ma and is 4.1 ± 0.4 km/s for Layer 2A, 5.2 ± 0.5 km/s for Layer 2B, and 5.9 ± 0.5 km/s for 1 km below the basement.

For Layer 2B velocities, we picked the velocities along the Layer 2A/2B boundary. As velocities picked near Layer 2A/2B boundary would give lower estimates of Layer 2B velocities due to smoothing effect in tomography, we also plot velocities 1 km below the basement at distinct ages. The age variation of the *P* velocities depicts most of the changes happening within the first 4 Myr with the velocities changing slightly thereafter. The Layer 2B velocities show greater variations than Layer 2A velocities. Unlike Layer 2A, there is continued increase of velocities in Layer 2B up to 46 Myr. This is followed by a slight decrease in velocities from 49–75 Ma similar to Layer 2A. We use a modification of the velocity-age variation proposed by Grevemeyer and Weigel (1996) to fit the velocities in Layers 2A and 2B. We obtain the following best fitting curves: $V_{2A} = 2.57 + 1.53erf(0.26t)$ km/s for Layer 2A (coefficient of determination, $r^2 = 0.87$ and root mean square error [r.m.s.e.] = 0.18 km/s), $V_{2B} = 4.53 + 0.7erf(0.19t)$ km/s for Layer 2B ($r^2 = 0.69$ and r.m.s.e. = 0.13 km/s), and $V = 4.78 + 1.14erf(0.22t)$ at 1 km below the basement ($r^2 = 0.88$ and r.m.s.e. = 0.12 km/s) where erf stands for error function and t is in Myr. These curves have been plotted in Figure 9, and their implications will be discussed in section 7.

6. Porosity Estimation

The increase of velocities with depth in the uppermost oceanic crust has been well known. There is lack of evidence of increasing metamorphic grade with depth in basalts (Andrews, 1977). There is also evidence that metamorphism may not necessarily increase the velocity of basalts (Christensen, 1970; Fox et al., 1973). The pressure and temperature variation of basalts are too small to be accounted for the increase in velocity with depth as observed (Murase and McBirney, 1973). Hence, the main predominating factor which can be accounted for the increase of velocity with depth in basalts is the pore and crack geometry. Wilkens et al. (1991) show the importance of aspect ratios of crack porosity on seismic velocities. According to this study, a small porosity reduction of a high aspect ratio crack will cause a greater increase in velocity as compared to the same porosity reduction of an spheroidal inclusion.

A differential effective medium aligned scheme (Taylor & Singh, 2002), first proposed by McLaughlin (1977), Cleary et al. (1980), and Norris (1985), is used to estimate a reliable *P* velocity-porosity relationship. The *P* velocity of zero-porosity basalt has been taken to be 6.74 km/s (Carlson, 2014b). The density of basalts has been taken as 2,930 kg/m^3 from modeling of borehole logs (Carlson, 2014a). The *S* velocity of zero-porosity basalt has been taken as 3.89 km/s assuming a Poisson's ratio of 0.25 from Collier and Singh (1998). The parameters for the circulating seawater have been taken as 1.5 km/s (*P* velocity), 0 km/s (*S* velocity), and 1,030 kg/m^3 (density). The effect on increasing the inclusion of seawater in pore spaces is seen on *P* velocity for different inverse aspect ratios (Figure S11). The inverse aspect ratio is the ratio of the polar to the equatorial radius and is a measure of how prolate the pore or the crack is. Figure S11 also shows the upper and lower bounds for the elastic moduli of basalt (Hashin & Shtrikman, 1963) using the parameter values described above. We did not consider age-related variations of density (Holmes & Johnson, 1993) and age-related variations of inverse aspect ratio to simplify the porosity computation.

An inverse aspect ratio of 5 gives Layer 2B porosities of 14% at zero age and in the range 7–11% at older ages with a mean of ~8%. This roughly coincides with the range of porosities modeled to fit borehole data which is 5.4–9.8% (Carlson, 2014a). A modification of the approximate model of the *P* velocity-porosity relation fit to borehole data from Carlson (2014a) is found to match the Layer 2B porosities quite well ($r^2 = 0.69$ and r.m.s.e. = 0.0098). The modified *P* velocity-porosity relation proposed is $\phi = (6.2 - V_p)0.089$ and has been plotted in Figure S11. Layer 2A porosities using the same inverse aspect ratio of 5 gives porosities ~ 40% at zero age and 16–21% elsewhere. The same *P* velocity-porosity relation for Layer 2A gives a poor fit with $r^2 = 0.14$ and r.m.s.e. = 0.0336. The zero age porosity of Layer 2A (40%) is almost double as compared to that of boreholes such as at the Endeavour segment which show porosities around 21% (Holmes & Johnson, 1993).

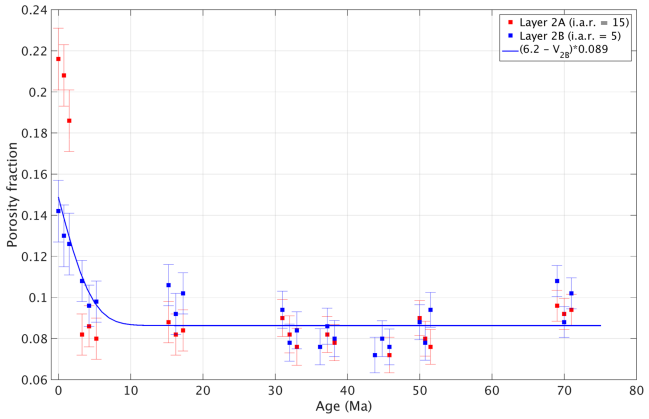

Figure 10. Layers 2A and 2B porosities plotted as a function of age. A differential effective medium aligned scheme (Figure S11) has been used to obtain porosities from *P* velocities from Figure 9 with an inverse aspect ratio (i.a.r.) of 15 for Layer 2A and 5 for Layer 2B which best fits borehole data. An approximate model fit to the borehole data (Carlson, 2014a) is also overlain and is a good match to the Layer 2B porosities.

Figure 10 shows the case when the inverse aspect ratio of Layer 2A is varied so that the obtained porosities lie in the same range as that of borehole results. An inverse aspect ratio of 5 for Layer 2B gives reasonable porosities as discussed above. The best fitting curve using Layer 2B *P* velocities and the P-velocity-porosity relation proposed above is also overlain. The *P* velocity-porosity relation proposed by Carlson and Herrick (1990) holds good for Layer 2B at zero age. For Layer 2A, an inverse aspect ratio of 15 gives porosities around 22% at zero age and ~8% elsewhere. The Layer 2A porosities are in good agreement with borehole results both at zero age and away from the ridge axis (Carlson, 2014a). The inverse aspect ratio estimated from borehole studies lie in the range 10–14 for modeling studies (Carlson, 2010). Hence, it can be stated that the difference in the velocities of Layers 2A and 2B is mainly due to difference in concentration of thin cracks and they may have similar porosities. Layer 2A has a higher concentration of thin cracks (inverse aspect ratio = 15), and as these cracks fill up, the velocity increases in Layer 2B, which in turn has a higher concentration of thicker cracks (inverse aspect ratio = 5).

7. Discussion

The results obtained in this study help in characterizing the evolution of an oceanic crust in a slow spreading regime over the age range of 0–75 Ma. Layer 2A is observed as a persistent feature of the upper oceanic crust with off-axis thinning and not much change in its velocities beyond 4 Ma (Figure 4b). Below, we will discuss different features from sediment cover to Layer 2B and how they affect evolution of the upper oceanic crust.

7.1. Sediment Cover

A rough basement morphology, which is typical of a slow spreading regime, is observed from the seismic profiles at all crustal ages (Figure 3). The sediment thickness increases rapidly for the first 4 Myr and decreases slightly up to 30 Myr and then again increases linearly up to 75 Myr (Figure 11), suggesting that the sediments up to 30 Myr are of pelagic origin, whereas those from 30–75 Myr might have turbiditic origin. Khripounoff et al. (2003) report activities of turbidity currents in the Congo-Angola continental shelf extending 760 km from the river mouth to the abyssal plain with a downslope of more than 5,100 m and covering an estimated area of 0.3×10^6 km^2. Ittekkot (1988) showed that 65% of the total organic matter is refractory and is carried into the deep ocean by midwater transport (Walsh, 1988), so it can be inferred that the eastern end of the seismic profile is under the influence of the Congo deep sea fan. We computed the sediment thickness from the sediment TWTT thickness and the velocities obtained from the RMS velocities as described in section 4 (Table S5). Figure 11 shows the variation of the thickness of sediments with age. A higher sediment thickness from 2–38 Myr and a lower sediment thickness in the rest of the profile is observed as compared to the global study of Whittaker et al. (2013). Decompacted sediments at the time of formation can be ~40% thicker as compared to the compacted sediments as observed today (Alibés et al., 1996). Agius et al. (2018) estimate the sediment velocity and thickness from 0–80 Ma old seafloor in the Equatorial Atlantic from *P*-to-*S* seismic phase conversion at the sediment-crust boundary and estimate sediment deposition rates of 5 mm/Kyr for seafloor younger than 10 Myr and 1.2 mm/Kyr for older seafloor. However, we observe much higher rates of sedimentation of 47 mm/Kyr for the first 4 Myr with the decompacted sediment thickness reaching a maximum of ~240 m for a compacted sediment thickness of ~170 m. This is in agreement with the IODP Leg 108 cores drilled on Sites 662 and 663 (Figure 1) (Ruddiman & Janecek, 1989), which sampled sediments to 200 m depth and estimated rates of deposition between 30 and 50 mm/Kyr (Ruddiman et al., 1989). We further examine the relationship between the

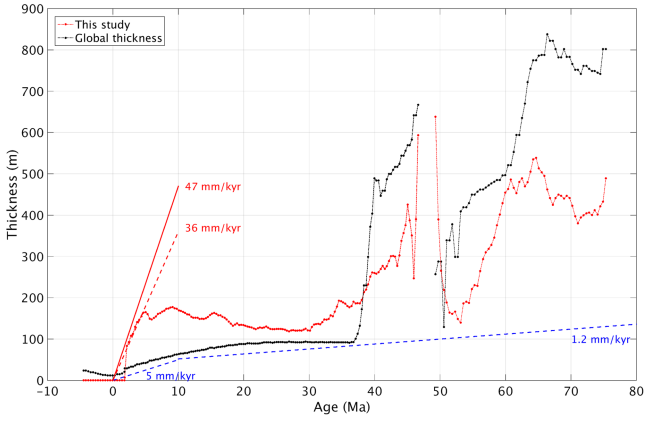

Figure 11. Variation of sediment thickness with age and comparison with global study (Whittaker et al., 2013). The uncertainty estimated for sediment thickness ranges from 20–50 m. The sedimentation rate for both compacted and decompacted sediments (Alibés et al., 1996) is also plotted in dashed red and solid red, respectively. Also shown in blue dashed lines are sediment deposition rates from Agius et al. (2018) in the Equatorial Atlantic from *P*-to-*S* seismic phase conversion at sediment-crust boundary.

paleosedimentation rates in the Atlantic, paleoclimatic conditions of northwestern Africa, and wind-driven coastal upwelling, the glacial-interglacial period, and oceanic productivity of organic matter (planktons) and the fluctuations in carbon dioxide reserves in the atmosphere and the deep ocean.

The high sedimentation rate (47 mm/Kyr) for the first 4 Myr could be due to increased glaciation (Ravelo et al., 2004) and/or high eolian dust fluxes from Africa to the Atlantic (Ruddiman et al., 1989). An expanded sea-ice cover in the high latitudes during the last glacial maximum led to a decrease in the ocean productivity of organic matter and caused wind-driven upwelling along the northeast Atlantic coast which in turn caused an increased ocean productivity in the lower latitudes. Furthermore, Sarnthein et al. (1988) proposed a near-surface large-scale lateral advection of organic matter from higher latitudes to lower latitudes which also caused lowering of the sea-surface temperatures. They also attribute the large-scale carbon dioxide depletion of the deep ocean reserves and the corresponding increase of atmospheric carbon dioxide to the onset of the deglaciation period wherein a decline of low-latitude upwelling and productivity was observed. Wagner (2000) found an increase in marine organic matter by 20–60% in the glacial conditions at Site 663 as compared to the interglacial conditions and related it to stronger oceanic upwelling during the late Quaternary glacial periods. North Africa exhibited arid climatic conditions since the Tortonian stage (~7–11 Ma) (Zhang et al., 2014), and the Passat and Harmattan wind systems are known to carry huge amounts of lithogenic dust in response to glacial-interglacial cycles from dry African areas to deep sea settings (deMenocal, 1995; deMenocal et al., 1993). More recently, the disintegration of the ice sheets during the last ~14,000 years and the resulting fresh water input to the oceans has been shown to decrease the productivity of the North Atlantic deep water and sea-surface temperature anomalies, creating extreme arid conditions in Northern Africa (Street-Perrott & Perrott, 1990). Wagner (2000) found a 60% increase in terrigenious organic matter at Site 663 during the glacial period corresponding to an increase in eolian dust fluxes. Total organic content has been found to be higher in upwelling site 658 as compared to nonupwelling sites 657 and 659 at the northwest African coast (Stein et al., 1986). The higher organic content is attributed to higher fluvial deposits and dense vegetation cover, prior to 3.1 Ma, after which northwestern Africa experienced more arid conditions.

However, the gradient slope in the sediment thickness with age between 10 and 30 Myr is difficult to explain. Strong bottom thermohaline intrusions as found in the North Atlantic deep waters (Sheen et al., 2012) could erode the sediments, decreasing the sediment thickness. Another possibility is that most of the sediments are deposited near the ridge axis by strong current within the ridge axis and upwelling and deposition of sediments just outside of the axial valley. In this scenario, there would have been a slight increase in the sedimentation between 30 and 5 Myr.

A thicker sediment cover beyond 35 Myr is observed where the sediment thickness almost doubles as compared to younger ages. The global sediment thickness map (Whittaker et al., 2013) also finds a sudden change starting at ~37 Ma, and the variation from 37–75 Ma in the sediment thickness is also similar to our results, although it overestimates the sediment thickness by 300–400 m as compared to our results. This increased sediment cover correlates well with the sedimentation flux history of the Congo river delta which shows a higher sediment flux from 2,500–3,000 km^3/Myr from 5–35 Myr to <500 km^3/Myr beyond 35 Myr (Paul et al., 2014).

7.2. Evolution of Layer 2A With Age

The Layer 2A is intermittently imaged at all the age profiles, suggesting that Layer 2A is present from 0–75 Ma. We find an increase in P velocity from 2.57 ± 0.28 km/s at zero age to 2.79 ± 0.28 km/s by ~1.5 Myr (Figure 9). The P velocity obtained at zero age at 35N MAR is 2.3 km/s and increases to >2.7 km/s within ~2 Myr (Hussenoeder et al., 2002). At 8–9S MAR, a mean Layer 2A velocity of 2.74 ± 0.24 km/s close to zero age has been obtained by modeling of wide-angle data (Minshull et al., 2003). At the Lucky Strike segment, zero-age velocities are found in the range 2.2–3 km/s (Arnulf et al., 2011), whereas Kardell et al. (2019) find velocities of ~2.4 km/s in the South Atlantic. A comparison of Layer 2A zero age P velocities is shown in Table 1. Our results at zero age are in good agreement with most of the studies in the slow-spreading MAR.

The top of the crust is always found to have velocities less than 4.5 km/s throughout the profile with velocities reaching 4.1 km/s within 4 Myr as shown in Figure 9. We find the best fitting curve to age variation of Layer 2A velocities as $V_{2A}(t) = 2.57 + 1.53erf(0.26t)$ km/s which matches well the data compiled by Grevemeyer and Weigel (1996). This increase of velocities is more rapid as that observed by Kardell et al. (2019), who observe velocities reaching ~4.2 km/s by 6 Ma. This rapid increase of velocities is attributed to active

Table 1
Comparison of Zero-Age Layer 2A P Velocity at Different Spreading Centers

Study	Spreading center	Zero age *P* velocity (km/s)
Hussenoeder, Kent, and Detrick (2002)	35 N MAR	2.3
Minshull et al. (2003)	8-9 S MAR	2.74
Arnulf et al. (2011)	Lucky Strike segment MAR	2.2-3
Kardell et al. (2019)	30 S MAR	2.4
Navin et al. (1998)	Reykjanes segment MAR	2.6
Nedimović et al. (2008)	Juan de Fuca Ridge	2.3-2.5
Hussenoeder, Detrick, et al. (2002)	17 S East Pacific Rise	2.1-2.4
This study	2 S MAR	2.57

Note. MAR is the slow-spreading Mid-Atlantic Ridge.

hydrothermal circulation and deposition of precipitates, leading to closure of the pore spaces. This is also related to rapid thickening of sediments within the first 4 Myr (Figure 11), which would act as a blanket and cease active hydrothermal circulation. The sediment blanketing could allow the hydrothermal fluids to stay longer in the crust and increasing the precipitate, as indicated by the increase of velocity. Kardell et al. (2019) also observe velocities reaching ~4.9 km/s at 58 Ma and propose low temperature hydrothermal circulation causing continuing evolution of Layer 2A. However, we find Layer 2A velocities become statistically constant at 4.1 ± 0.4 km/s beyond 4 Myr, similar to Grevemeyer and Weigel (1996). A clear trend could not be identified beyond 4 Ma as the velocities show a slight decrease at 16 Myr and an increase at 35–45 Myr with a local effect reducing the velocities at 75 Ma. A local effect causes reduction of the velocities to ~3.8 km/s near 70 Ma and may be due to passive hydrothermal circulation. Passive, off-axis hydrothermal circulation is characterized by low Rayleigh numbers indicating a much steady flow as compared to the turbulent flow observed in on-axis active hydrothermal systems. We do not observe passive hydrothermal circulation to affect Layer 2A velocities elsewhere. Fluid circulation has been demonstrated in crust as old as 106 Ma on the Atlantic ocean floor (Fisher & Von Herzen, 2005). We observe slightly lower Layer 2A velocities as compared to Kardell et al. (2019) which indicates a difference in evolution of the African Plate in the Equatorial Atlantic and the South American Plate in the South Atlantic.

The porosity and inverse aspect ratio estimates in Figure 10 further help in providing additional information on the evolution of the crust. Our estimated layer 2A porosities with inverse aspect ratio of 15 (figure 10) show good match with gravity-based estimates (Holmes & Johnson, 1993; Grevemeyer & Bartetzko, 2004) and borehole data (Carlson, 2014a). Based on seafloor gravity data, (Grevemeyer & Bartetzko, 2004) find a decrease in porosity in uppermost oceanic crust to 10% by 15 Kyr, and no correlation between age and porosity is inferred beyond 0.2 Ma (Carlson, 2014a). We find that like Layer 2A velocities, most of the changes in Layer 2A porosities take place near the ridge axis and do not show much variations thereafter.

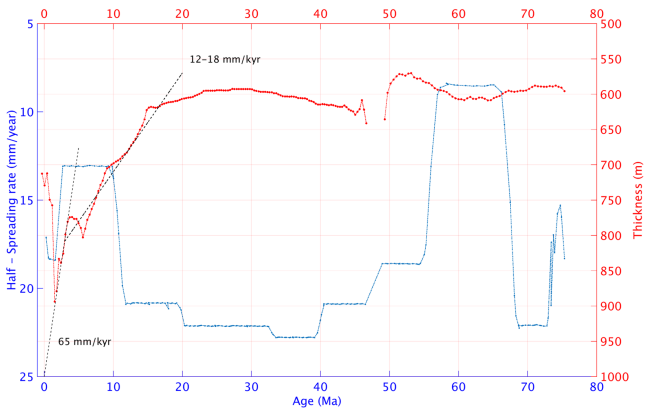

Figure 12. Variation of Layer 2A thickness (red) with age and half-spreading rate (blue) (Müller et al., 2008) in the Equatorial Atlantic. Black dashed lines show two distinct thinning rates which have been identified as corresponding to the distinct age ranges. The upper bound of uncertainty on the thickness of Layer 2A is ±365 m (±315 m at zero age) and is found in regions of rugged bathymetry and the lower bound of uncertainty in regions of flatter bathymetry is ±165 m.

7.3. Variation of Layer 2A Thickness With Age

The seismic TWTT thickness of layer 2A decreases from 500 ± 70 ms at the ridge axis to 300 ± 30 ms at 75 Ma (Figure 4b). Regions having a flat basement provide good opportunities to image the Layer 2A event and to best constrain its thickness. Local thickening and thinning of the seismic Layer 2A are observed beneath bathymetric valleys and seamounts as seen in Figure 3. We used the tomography Layer 2A velocities from Figure 9 and the Layer 2A TWTT thickness from Figure 4b to obtain the physical thickness of Layer 2A. Figure 12 shows the variation of Layer 2A thickness with age. At the ridge axis, the thickness of Layer 2A is variable and lies in the range of 800–900 m ± 315 m with the maximum thickness being ~900 m at ~1 Ma. This is close to thickness estimated at the Lucky Strike segment of the MAR (Combier et al., 2015), the hot spot influenced Reykjanes segment (Navin et al., 1998), and near the Ascension islands (Minshull et al., 2003). Estep et al. (2019) estimate Layer 2A thickness of

~1,000 m near the ridge axis and estimate a mean thickness of 759 ± 326 m for crust aged 0–7 Myr in the South Atlantic. They do not observe Layer 2A thinning systematically with age and find an increase in Layer 2A thickness at 15–31 Ma, whereas we find a decrease in Layer 2A thickness from a maximum of ~900 m near the ridge axis to ~770 m at 4 Myr and estimate a thinning rate of 65 mm/Kyr. A clear trend is not seen from 4–15 Myr, and we estimate thinning rates of 12–18 mm/Kyr. Beyond 15 Myr, there is not much change in the Layer 2A thickness, and we estimate thickness in the range of 570–620 m with an uncertainty ranging from ±365 to ±165 m. These are similar to off-axis thickness of Layer 2A observed elsewhere. However, Estep et al. (2019) do not observe layer 2A event in the seismic beyond 48 Myr which they attribute to rough basement topography and/or the closure of pore spaces lying below the threshold to be seen in seismic records. These studies including our results suggest that thickness of Layer 2A is established at the ridge axis in slow spreading centers such as MAR. Unlike fast spreading ridges such as East Pacific rise where a rapid thickening takes place (Harding et al., 1993; Vera & Diebold, 1994) or at intermediate spreading centers such as Juan de Fuca ridge (Canales et al., 2005) and Galapagos spreading center (Blacic et al., 2004) where gradual off-axis thickening is observed, our results indicate that off-axis thinning is observed in slow spreading centers and off-axis thickness of Layer 2A (~600 m) is similar to those at other spreading centers (Hussenoeder et al., 2002).

The off-axis thinning of Layer 2A at slow spreading ridges can be explained by considering seawater circulating to greater depths at the ridge axis where no sediments are present and the upper crust is faulted due to tectonic extension (Figure 3a). Heat from base of the lithosphere would be higher as it is shallower near the ridge axis and would result in precipitation of minerals at depths corresponding to Layer 2A/2B boundary observed in this study. Away from the ridge axis, a rapidly thickening sediment cover accompanied by reduced heat supply due to subsidence of the base of lithosphere may restrict the depths of penetration of the hydrothermal fluids. The regime from 0–4 Myr may be influenced by active hydrothermal circulation which decreases away from the ridge axis, and passive hydrothermal circulation may influence the crust from 4–15 Myr. An alternate explanation attributes the off-axis thinning to tectonic reasons with the Layer 2A erupted as a volcanic mound at the ridge axis and then faulted, thinned, and transported off-axis (Combier et al., 2015; Macdonald, 1982).

The above quantification of thinning of Layer 2A is valid assuming the spreading rate is independent of Layer 2A thickness and most of the crustal thickness variations are linked to lower crustal (Layer 3) thickness variations, as proposed by Mutter and Mutter (1993). Slow spreading rates are observed at 3–10 Myr, ultraslow spreading rate at 57–65 Myr, and intermediate spreading rates at 12–46 Myr for the study region as computed by Müller et al. (2008). We correlate the Layer 2A thickness with the spreading rate as shown in Figure 12 to examine their relation. If the thickness of Layer 2A were completely produced at the ridge axis and unaffected by hydrothermal circulation, there must be a correlation between the spreading rate and the Layer 2A thickness. We do not observe any correlation between the spreading rates and the Layer 2A thickness, and hence, hydrothermal circulation has to be accounted for the thinning of the Layer 2A. It is fair to assume a uniformly thick Layer 2A being produced at the ridge axis with hydrothermal circulation thinning Layer 2A to different degrees depending on whether it is in younger crust (active) or older crust (passive).

7.4. Evolution of Layer 2B With Age

The base of Layer 2A, which is considered to be a hydrothermal alteration boundary, shows an increase in velocities ranging from ~4.5 km/s at zero age to a maximum of ~5.5 km/s in older oceanic crust (Figure 9). We found the best fitting curve for Layer 2B velocities as $V_{2B}(t) = 4.53+0.7erf(0.19t)$ km/s from Grevemeyer and Weigel (1996). Similar to Layer 2A, the velocities in Layer 2B are found to increase from ~4.5 km/s at zero age to 5.1 km/s at 4 Myr. Whereas velocities in Layer 2A become statistically constant at 4.1 ± 0.4 km/s beyond 4 Myr, velocities in Layer 2B show slightly more variations. We find a gradual increase from ~5.1 km/s at 4 Myr to a maximum of ~5.5 km/s at 36–46 Myr, which could be due to an off-axis increase in the depth of penetration of the circulating fluids involved in hydrothermal circulation. This increase in velocities is followed by the lowering of velocities to ~5.2 km/s at 51 and 70 Myr. In the South Atlantic, Kardell et al. (2019) observe Layer 2B velocities of 5 km/s close to the ridge axis, which varies slightly within the first 12 Myr and find velocities reaching 5.5 km/s more rapidly at ~20 Myr. At the intermediate spreading Juan de Fuca ridge, Newman et al. (2011) propose a rapid evolution of Layer 2B velocities to 5.2 ± 0.3 km/s within 0.5 Myr from crustal formation. However, Christeson et al. (2012) finds velocities in upper part of Layer 2B in the range 4.7–4.9 km/s with an average value of 4.8 ± 0.25 km/s at young fast and intermediate spreading centers. The inconsistent values of Layer 2B velocities in these studies may be due to differences

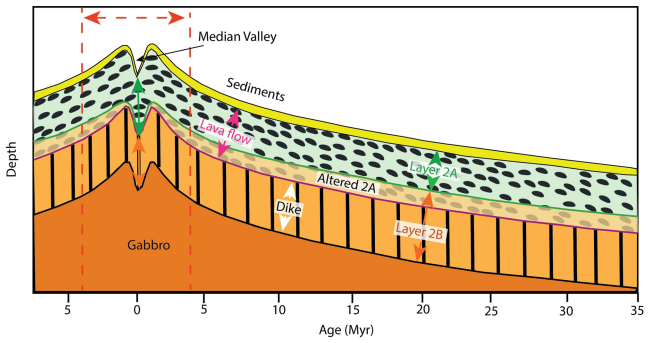

Figure 13. Schematic diagram showing Layer 2A thinning but persisting as lava flow at mature crustal ages. The magenta double arrow represents the lava flow, and the green double arrow represents the Layer 2A which thins away from the ridge axis due to hydrothermal circulation. The solid green line denotes the hydrothermal alteration front, and solid magenta line denotes the top of the sheeted dykes. Active hydrothermal circulation is limited to first 4 Myr (dashed red lines), after which passive hydrothermal circulation becomes dominant. After 15 Myr, hydrothermal circulation stops thinning the Layer 2A, although fluid circulation may continue with the basement outcrops serving as recharge and discharge sites. The Layer 2A/2B boundary is a lava/dike contact at the ridge axis, whereas it is a hydrothermal alteration boundary above the dikes in older crust. Note that the image is not to scale.

in methods of estimation or due to differences in geological settings of the regions. The range of Layer 2B velocities beyond 4 Myr observed in this study can be approximated as 5.2 ± 0.5 km/s, which is close to the data compiled by Houtz and Ewing (1976), who estimate mean Layer 2B velocities in the Atlantic as 5.13 ± 0.38 km/s and matches with the observed velocities at Juan de Fuca (Newman et al., 2011).

An important observation is that we do not find velocities at top of Layer 2B exceeding 5.8 km/s, which is the lowest velocity observed in dikes at Boreholes 504B and 1256D Carlson (2014a). This is also found from seismic data compiled by (Carlson, 2018), who proposes the dike section to be Layer 2C as originally observed by Houtz and Ewing (1976). At depths of 1 km below the basement, we find velocities in the range 4.8–5.1 km/s at the ridge axis and a more variable 5.5–6.2 km/s at older ages from Figure 9. This implies that the dike section is reached within 1 km below the top of the crust. The lower velocities in the dike section at zero age are possibly due to higher temperatures near the ridge axis and are close to velocities observed at the 2A/2B boundary. The distinction between 2A/2B velocities and velocities 1 km below basement becomes clear away from the ridge axis. We find the best fitting curve $V(t) = 4.78 + 1.14erf(0.22t)$ for velocities 1 km below the basement which become statistically constant at 5.9 ± 0.5 km/s beyond 4 Myr. Additionally, estimated porosities for Layer 2B (Figure 10) using an inverse aspect ratio of 5 show a good match to the porosities in the extrusive section observed in boreholes (Carlson, 2014a). Hence, it would be safe to conclude from our results that the Layer 2A/2B boundary could be a lava/dike transition at the ridge axis and a hydrothermal alteration boundary within the extrusive section away from the ridge.

The zero-age porosity for Layer 2A is ∼21% which decreases to ∼14% at depths of ∼850 m corresponding to Layer 2A/2B boundary. At the Reykjanes Ridge segment of the MAR, the crustal porosity has been found to decrease from ∼25% to ∼7% at 1 km depth (Greer et al., 2002). At other ages, porosities of Layers 2A and 2B lie in the range observed in boreholes (Carlson, 2010). As mentioned in section 6, the inverse aspect ratio used in computing the porosities for Layers 2A and 2B has been adjusted to fit the borehole observations. The increase in velocity from Layer 2A to Layer 2B may then be caused by a change in the concentration of thin cracks. The filling up of thin cracks in Layer 2A (inverse aspect ratio of 15) due to hydrothermal alteration would produce a relatively large velocity increase (Wilkens et al., 1991), while Layer 2B would be populated with more thicker cracks (inverse aspect ratio of 5).

7.5. Implications of This Study

The results of this study indicate the possibility of a continuous hydrothermal system from the ridge axis to the mature oceanic crust (∼15 Ma) with passive hydrothermal circulation systems becoming dominant beyond 4 Ma (Figure 13). The active hydrothermal systems found near the ridge axis, which are associated with smoker fields and high temperature vents cause a rapid increase in Layer 2A velocities. The high sedimentation rate away from the ridge axis would restrict the depth of penetration of the hydrothermal fluids and thereby reducing the Layer 2A thickness. Off-axis, heat from the base of lithosphere is reducing due to cooling of the lithospheric plate leading to passive hydrothermal circulation, which is found to be dominant beyond 4 Myr and until 15 Myr at which Layer 2A reaches typical off-axis thickness values. This heat from the base of the lithosphere may also metamorphose Layer 2A basalts and hence decrease its thickness. A gradual increase in Layer 2B velocities in observed until ∼46 Myr, which may be due to depth of the hydrothermally circulating fluids. Recent results of the Oman drilling project (Harris et al., 2017) have found evidence of a hydrothermally altered lower crust indicating the depth of penetration of hydrothermal fluids in the lower crust. The Layer 2A/2B boundary is proposed to be a lava/dike transition on-axis and a hydrothermal alteration boundary within the extrusive section off-axis. Our results match well with the model proposed by Shaw (1994), in which the thin cracks preferentially close at shallow depths (in Layer 2A) in young oceanic crust by hydrothermal alteration while thicker cracks at greater depths (Layer 2B) gradually seal with age also by hydrothermal deposition. This explains the gradual increase of Layer 2B velocities with age and Layer 2A having thinner cracks as compared to Layer 2B.

Fluid circulation may continue in the basement beyond 15 Myr without significantly influencing Layer 2A velocities and thickness. Basement outcrops, having higher permeability (10^{-13} m^2) than sediments (10^{-15} m^2), act as discharge and recharge sites for passive hydrothermal systems and fluid circulation (Harris et al., 2004; Villinger et al., 2002). A number of these basement outcrops can be found from the 3-D global bathymetry grid. The recharge and discharge outcrops can be separated by as much as 50 km as observed at the (Juan de Fuca Ridge Fisher et al., 2003). Apart from Kardell et al. (2019) who support the idea of long lasting hydrothermal circulation, Baker et al. (1991) suggest a large-scale lateral advection of seawater through basaltic oceanic crust on the basis of isotopic pore water composition of overlying sediments in equatorial Pacific ocean over an age spanning 15 to 70 Ma. Anomalous heat flow values have been found at 83 Ma Atlantic seafloor (Embley et al., 1983), and models of hydrothermal circulation have been demonstrated to be consistent with observations in crust as old as 106 Ma in the Atlantic (Fisher & Von Herzen, 2005).

8. Conclusions

We have presented a seismic data analysis of ~1,500 km long profile in the equatorial Atlantic Ocean with ~560 km of high-resolution *P* velocity models spanning an age range of 0–75 Ma. Along with the recent results of Kardell et al. (2019) and Estep et al. (2019) on the South America plate, our results provide a global view of the upper crustal structure in the Central Atlantic Ocean. The major conclusions from our study are as follows:

1. The sediment cover increases rapidly to 170 m within the first 4 Myr with an estimated rate of deposition of 47 mm/Kyr and then varies slightly until 30 Ma. These are of pelagic origin, whereas the sudden thickening of sediments beyond 30 Ma are of turbiditic origin.
2. The uppermost layer of oceanic crust, Layer 2A, is found to persist from 0–75 Ma old crust. The increase in velocities is rapid from 2.5 km/s at zero age ridge axis to 4.1 km/s at 4 Ma and varies slightly thereafter. Porosities derived from *P* velocities decrease from 21% at the ridge axis to 7–9% at older ages assuming an inverse aspect ratio of 15. Active hydrothermal circulation is attributed to the rapid increase in velocities during the first 4 Myr. This is also related to the thickening of sediments near the ridge axis, suggesting the cessation of active hydrothermal circulations is linked to blanketing by sediments. Passive hydrothermal circulation is found to dominate from there onward until 15 Myr and may also locally affect the velocities beyond 15 Myr.
3. Layer 2B shows an increase in velocities from 4.5 to 5.1 km/s within the first 4 Ma. There is a gradual increase to 5.5 km/s until ~46 Ma which may be due to a local effect of passive hydrothermal circulation and indicates the depth of penetration of the hydrothermal fluids. There is a decrease in porosities from 14% at the ridge axis to 7–11% at older ages using an inverse aspect ratio of 5.
4. Velocities 1 km below the basement are similar to velocities at top of Layer 2B at the ridge axis. Away from the ridge axis, they are higher than 2B velocities and lie in the range of velocities of dikes observed in boreholes. The boundary between Layers 2A and 2B likely represents a lava/dike transition at the ridge axis, whereas away from the ridge axis, it corresponds to a hydrothermal alteration boundary within the extrusive section. Layer 2A consists of thin cracks, while Layer 2B consists of relatively 3 times thicker cracks.
5. The decrease in Layer 2A thickness is from ~850 m at the ridge axis to ~600 m at 50 Ma. Two distinct thinning rates have been computed for Layer 2A: 65 mm/kyr for 0–4 Ma and 12–18 mm/Kyr from 4–15 Ma. These distinct thinning rates imply how the effect of hydrothermal circulation varies as we move to the older ages.

Acknowledgments
This research has been funded by ERC Advance Grant Agreement 339442 TransAtlanticILAB. A data set including the digital seafloor, basement, and Layer 2A picks for the whole profile (https://doi.org/10.1594/IEDA/326177) along with the processed seismic data showing Layer 2A (https://doi.org/10.1594/IEDA/326175) is available to the public on the repository Marine Geosciences Data System (http://www.marine-geo.org/index.php). Helpful reviews from Richard Carlson and an anonymous reviewer substantially improved the article.

References

Agius, M., Harmon, N., Rychert, C., Tharimena, S., & Kendall, J.-M. (2018). Sediment characterization at the equatorial Mid-Atlantic Ridge from *P*-to-*S* teleseismic phase conversions recorded on the PI-LAB Experiment. *Geophysical Research Letters*, *45*, 12,244–12,252. https://doi.org/10.1029/2018GL080565

Alibés, B., Canals, M., Alonso, B., Lebreiro, S., & Weaver, P., (1996). Quantification of Neogene and Quaternary sediment input to the Madeira Abyssal Plain. *Geogaceta*, *20*(2), 394–397.

Alt, J. C., Laverne, C., Coggon, R. M., Teagle, D. A., Banerjee, N. R., Morgan, S., et al. (2010). Subsurface structure of a submarine hydrothermal system in ocean crust formed at the East Pacific Rise, ODP/IODP site 1256. *Geochemistry, Geophysics, Geosystems*, *11*, Q10010. https://doi.org/10.1029/2010GC003144

Andrews, A. (1977). Low temperature fluid alteration of oceanic layer 2 basalts, DSDP leg 37. *Canadian Journal of Earth Sciences*, *14*(4), 911–926.

Arnulf, A., Singh, S., Harding, A., Kent, G., & Crawford, W. (2011). Strong seismic heterogeneity in layer 2a near hydrothermal vents at the Mid-Atlantic Ridge. *Geophysical Research Letters*, *38*, L13320. https://doi.org/10.1029/2011GL047753

Baker, P. A., Stout, P. M., Kastner, M., & Elderfield, H. (1991). Large-scale lateral advection of seawater through oceanic crust in the central equatorial Pacific. *Earth and Planetary Science Letters*, *105*(4), 522–533.

Berryhill, J. R. (1984). Wave-equation datuming before stack. *Geophysics*, *49*(11), 2064–2066.

Bird, P. (2003). An updated digital model of plate boundaries. *Geochemistry, Geophysics, Geosystems*, *4*(3), 1027. https://doi.org/10.1029/2001GC000252

Blacic, T. M., Ito, G., Canales, J. P., Detrick, R. S., & Sinton, J. (2004). Constructing the crust along the Galapagos Spreading Center 91.3°–95.5°W: Correlation of seismic layer 2a with axial magma lens and topographic characteristics. *Journal of Geophysical Research*, *109*, B10310. https://doi.org/10.1029/2004JB003066

Bonatti, E. (1996). Anomalous opening of the equatorial Atlantic due to an equatorial mantle thermal minimum. *Earth and Planetary Science Letters*, *143*(1-4), 147–160.

Bonatti, E., Peyve, A., Kepezhinskas, P., Kurentsova, N., Seyler, M., Skolotnev, S., & Udintsev, G. (1992). Upper mantle heterogeneity below the Mid-Atlantic Ridge, 0–15° N. *Journal of Geophysical Research*, *97*(B4), 4461–4476.

Canales, J. P., Detrick, R. S., Carbotte, S. M., Kent, G. M., Diebold, J. B., Harding, A., et al. (2005). Upper crustal structure and axial topography at intermediate spreading ridges: Seismic constraints from the Southern Juan de Fuca Ridge. *Journal of Geophysical Research*, *110*, B12104. https://doi.org/10.1029/2005JB003630

Carlson, R. (1998). Seismic velocities in the uppermost oceanic crust: Age dependence and the fate of layer 2a. *Journal of Geophysical Research*, *103*(B4), 7069–7077.

Carlson, R. (2010). How crack porosity and shape control seismic velocities in the upper oceanic crust: Modeling downhole logs from holes 504B and 1256D. *Geochemistry, Geophysics, Geosystems*, *11*, Q04007. https://doi.org/10.1029/2009GC002955

Carlson, R. (2011). The effect of hydrothermal alteration on the seismic structure of the upper oceanic crust: Evidence from holes 504B and 1256D. *Geochemistry, Geophysics, Geosystems*, *12*, Q09013. https://doi.org/10.1029/2011GC003624

Carlson, R. (2014a). The influence of porosity and crack morphology on seismic velocity and permeability in the upper oceanic crust. *Geochemistry, Geophysics, Geosystems*, *15*, 10–27. https://doi.org/10.1002/2013GC004965

Carlson, R. (2014b). The effects of alteration and porosity on seismic velocities in oceanic basalts and diabases. *Geochemistry, Geophysics, Geosystems*, *15*, 4589–4598. https://doi.org/10.1002/2014GC005537

Carlson, R. (2018). Ocean crustal seismic layer 2c. *Geochemistry, Geophysics, Geosystems*, *19*, 3084–3096. https://doi.org/10.1029/2018GC007614

Carlson, R., & Herrick, C. (1990). Densities and porosities in the oceanic crust and their variations with depth and age. *Journal of Geophysical Research*, *95*(B6), 9153–9170.

Christensen, N. I. (1970). Possible greenschist facies metamorphism of the oceanic crust. *Geological Society of America Bulletin*, *81*(3), 905–908.

Christensen, N. I., & Salisbury, M. H. (1972). Sea floor spreading, progressive alteration of layer 2 basalts, and associated changes in seismic velocities. *Earth and Planetary Science Letters*, *15*(4), 367–375.

Christeson, G. L., Karson, J. A., & McIntosh, K. D. (2010). Mapping of seismic layer 2A/2B boundary above the sheeted dike unit at intermediate spreading crust exposed near the Blanco Transform. *Geochemistry, Geophysics, Geosystems*, *11*, Q03015. https://doi.org/10.1029/2009GC002864

Christeson, G. L., Kent, G., Purdy, G., & Detrick, R. (1996). Extrusive thickness variability at the East Pacific Rise, 9°–10° N Constraints from seismic techniques. *Journal of Geophysical Research*, *101*(B2), 2859–2873.

Christeson, G. L., McIntosh, K. D., & Karson, J. A. (2007). Inconsistent correlation of seismic layer 2a and lava layer thickness in oceanic crust. *Nature*, *445*(7126), 418.

Christeson, G. L., Morgan, J. V., & Warner, M. R. (2012). Shallow oceanic crust: Full waveform tomographic images of the seismic layer 2a/2b boundary. *Journal of Geophysical Research*, *117*, B05101. https://doi.org/10.1029/2011JB008972

Cleary, M. P., Lee, S.-M., & Chen, I.-W. (1980). Self-consistent techniques for heterogeneous media. *Journal of the Engineering Mechanics Division*, *106*(5), 861–887.

Cogné, J.-P., & Humler, E. (2004). Temporal variation of oceanic spreading and crustal production rates during the last 180 my. *Earth and Planetary Science Letters*, *227*(3-4), 427–439.

Collier, J., & Singh, S. (1998). Poisson's ratio structure of young oceanic crust. *Journal of Geophysical Research*, *103*(B9), 20,981–20,996.

Combier, V., Seher, T., Singh, S. C., Crawford, W. C., Cannat, M., Escartín, J., & Dusunur, D. (2015). Three-dimensional geometry of axial magma chamber roof and faults at Lucky Strike volcano on the Mid-Atlantic Ridge. *Journal of Geophysical Research: Solid Earth*, *120*, 5379–5400. https://doi.org/10.1002/2015JB012365

deMenocal, P. B. (1995). Plio-Pleistocene African climate. *Science*, *270*(5233), 53–59. https://doi.org/10.1126/science.270.5233.53

deMenocal, P. B., Ruddiman, W. F., & Pokras, E. M. (1993). Influences of high- and low-latitude processes on African terrestrial climate: Pleistocene eolian records from equatorial Atlantic ocean drilling program site 663. *Paleoceanography*, *8*, 209–242. https://doi.org/10.1029/93PA02688

DeMets, C., Gordon, R. G., & Argus, D. F. (2010). Geologically current plate motions. *Geophysical Journal International*, *181*(1), 1–80.

Detrick, R., Collins, J., Stephen, R., & Swift, S. (1994). In situ evidence for the nature of the seismic layer 2/3 boundary in oceanic crust. *Nature*, *370*(6487), 288.

Dunn, R. A., Lekić, V., Detrick, R. S., & Toomey, D. R. (2005). Three-dimensional seismic structure of the Mid-Atlantic Ridge (35° N): Evidence for focused melt supply and lower crustal dike injection. *Journal of Geophysical Research*, *110*, B09101. https://doi.org/10.1029/2004JB003473

Embley, R. W., Hobart, M. A., Anderson, R. N., & Abbott, D. (1983). Anomalous heat flow in the Northwest Atlantic: A case for continued hydrothermal circulation in 80-my crust. *Journal of Geophysical Research*, *88*(B2), 1067–1074.

Estep, J., Reece, R., Kardell, D. A., Christeson, G. L., & Carlson, R. L. (2019). Seismic layer 2a: Evolution and thickness from 0- to 70-ma crust in the slow-intermediate spreading South Atlantic. *Journal of Geophysical Research: Solid Earth*, *124*, 7633–7651. https://doi.org/10.1029/2019JB017302

Fisher, A., Davis, E., Hutnak, M., Spiess, V., Zühlsdorff, L., Cherkaoui, A., et al. et al. (2003). Hydrothermal recharge and discharge across 50 km guided by seamounts on a young ridge flank. *Nature*, *421*(6923), 618.

Fisher, A. T., & Von Herzen, R. P. (2005). Models of hydrothermal circulation within 106 ma seafloor: Constraints on the vigor of fluid circulation and crustal properties, below the Madeira Abyssal Plain. *Geochemistry, Geophysics, Geosystems*, *6*, Q11001. https://doi.org/10.1029/2005GC001013

Fox, P. J., Schreiber, E., & Peterson, J. (1973). The geology of the oceanic crust: Compressional wave velocities of oceanic rocks. *Journal of Geophysical Research*, *78*(23), 5155–5172.

Granot, R., & Dyment, J. (2015). The cretaceous opening of the South Atlantic Ocean. *Earth and Planetary Science Letters*, *414*, 156–163.

Greer, A. A., Sinha, M. C., & MacGregor, L. M. (2002). Joint effective medium modelling for co-incident seismic and electromagnetic data, and its application to studies of porosity structure at mid-ocean ridge crests. *LITHOS Science Report*, *4*, 103–120.

Grevemeyer, I., & Bartetzko, A. (2004). Hydrothermal ageing of oceanic crust: Inferences from seismic refraction and bore hole studies. In *Hydrogeology of Oceanic Lithosphere* (pp. 128–150). Cambridge: Cambridge University Press.

Grevemeyer, I., & Weigel, W. (1996). Seismic velocities of the uppermost igneous crust versus age. *Geophysical Journal International*, *124*(2), 631–635.

Hansen, P. C., & O'Leary, D. P. (1993). The use of the L-curve in the regularization of discrete ill-posed problems. *SIAM Journal on Scientific Computing*, *14*(6), 1487–1503.

Harding, A. J., Kent, G. M., Orcutt, J., et al. (1993). A multichannel seismic investigation of upper crustal structure at 9° N on the East Pacific Rise: Implications for crustal accretion. *Journal of Geophysical Research*, *98*(B8), 13,925–13,944.

Harris, M., B. Zihlmann, D. Mock, T. Akitou, D. A. H. Teagle, K. Kondo, et al.nd et al. (2017), Hydrothermal alteration of the lower oceanic crust: Insight from OmanDP Holes GT1A and GT2A, AGU Fall Meeting Abstracts.

Harris, R. N., Fisher, A. T., & Chapman, D. S. (2004). Fluid flow through seamounts and implications for global mass fluxes. *Geology*, *32*(8), 725–728.

Hashin, Z., & Shtrikman, S. (1963). A variational approach to the theory of the elastic behaviour of multiphase materials. *Journal of the Mechanics and Physics of Solids*, *11*(2), 127–140.

Hasterok, D. (2013). A heat flow based cooling model for tectonic plates. *Earth and Planetary Science Letters*, *361*, 34–43.

Hasterok, D., Chapman, D., & Davis, E. (2011). Oceanic heat flow: Implications for global heat loss. *Earth and Planetary Science Letters*, *311*(3-4), 386–395.

Hill, M. (1957). Recent geophysical exploration of the ocean floor. *Physics and Chemistry of the Earth*, *2*, 129–163.

Holmes, M. L., & Johnson, H. P. (1993). Upper crustal densities derived from sea floor gravity measurements: Northern Juan de Fuca Ridge. *Geophysical Research Letters*, *20*(17), 1871–1874.

Houtz, R., & Ewing, J. (1976). Upper crustal structure as a function of plate age. *Journal of Geophysical Research*, *81*(14), 2490–2498.

Hussenoeder, S. A., Kent, G. M., & Detrick, R. S. (2002). Upper crustal seismic structure of the slow spreading Mid-Atlantic Ridge, 35° N: Constraints on volcanic emplacement processes. *Journal of Geophysical Research*, *107*(B8), 2156. https://doi.org/10.1029/2001JB001691

Ittekkot, V. (1988). Global trends in the nature of organic matter in river suspensions. *Nature*, *332*(6163), 436.

Kardell, D. A., Christeson, G. L., Estep, J. D., Reece, R. S., & Carlson, R. L. (2019). Long-lasting evolution of layer 2a in the western South Atlantic: Evidence for low-temperature hydrothermal circulation in old oceanic crust. *Journal of Geophysical Research: Solid Earth*, *124*, 2252–2273. https://doi.org/10.1029/2018JB016925

Karson, J. A. (2002). Geologic structure of the uppermost oceanic crust created at fast-to intermediate-rate spreading centers. *Annual Review of Earth and Planetary Sciences*, *30*(1), 347–384.

Karson, J. A., & Christeson, G. L. (2003). Comparisonic crust: Insights from a crustal cross-section at the hess deep rift. In *Heterogeneity in the Crust and Upper Mantle* (pp. 99–129). Boston, MA: Springer.

Khripounoff, A., Vangriesheim, A., Babonneau, N., Crassous, P., Dennielou, B., & Savoye, B. (2003). Direct observation of intense turbidity current activity in the zaire submarine valley at 4000 m water depth. *Marine Geology*, *194*(3-4), 151–158.

Le Pichon, X., Houtz, R., Drake, C. L., & Nafe, J. E. (1965). Crustal structure of the mid-ocean ridges: 1 Seismic refraction measurements. *Journal of Geophysical Research*, *70*(2), 319–339.

Lewis, B. (1978). Evolution of ocean crust seismic velocities. *Annual Review of Earth and Planetary Sciences*, *6*(1), 377–404.

Macdonald, K. C. (1982). Mid-ocean ridges: Fine scale tectonic, volcanic and hydrothermal processes within the plate boundary zone. *Annual Review of Earth and Planetary Sciences*, *10*(1), 155–190. https://doi.org/10.1146/annurev.ea.10.050182.001103

McLaughlin, R. (1977). A study of the differential scheme for composite materials. *International Journal of Engineering Science*, *15*(4), 237–244.

Minshull, T., Bruguier, N., & Brozena, J. (2003). Seismic structure of the Mid-Atlantic Ridge, 8–9° S. *Journal of Geophysical Research*, *108*(B11), 2513. https://doi.org/10.1029/2002JB002360

Morgan, J. P., & Chen, Y. J. (1993). The genesis of oceanic crust: Magma injection, hydrothermal circulation, and crustal flow. *Journal of Geophysical Research*, *98*(B4), 6283–6297.

Moser, T., Nolet, G., & Snieder, R. (1992). Ray bending revisited. *Bulletin of the Seismological Society of America*, *82*(1), 259–288.

Müller, R. D., Sdrolias, M., Gaina, C., & Roest, W. R. (2008). Age, spreading rates, and spreading asymmetry of the world's ocean crust. *Geochemistry, Geophysics, Geosystems*, *9*, Q04006. https://doi.org/10.1029/2007GC001743

Murase, T., & McBirney, A. R. (1973). Properties of some common igneous rocks and their melts at high temperatures. *Geological Society of America Bulletin*, *84*(11), 3563–3592.

Mutter, C., & Mutter, J. (1993). Variations in thickness of layer 3 dominate oceanic crustal structure. *Earth and Planetary Science Letters*, *117*, 295–317. https://doi.org/10.1016/0012-821X(93)90134-U

Navin, D., Peirce, C., & Sinha, M. (1998). The RAMESSES experiment–II Evidence for accumulated melt beneath a slow spreading ridge from wide-angle refraction and multichannel reflection seismic profiles. *Geophysical Journal International*, *135*(3), 746–772.

Newman, K. R., Nedimović, M. R., Canales, J. P., & Carbotte, S. M. (2011). Evolution of seismic layer 2b across the juan de fuca ridge from hydrophone streamer 2-D traveltime tomography. *Geochemistry, Geophysics, Geosystems*, *12*, Q05009. https://doi.org/10.1029/2010GC003462

Norris, A. (1985). A differential scheme for the effective moduli of composites. *Mechanics of Materials*, *4*(1), 1–16.

Olson, C. J., J. J. Becker, and D. T. Sandwell (2014), A new global bathymetry map at 15 arcsecond resolution for resolving seafloor fabric: SRTM15_PLUS, AGU Fall Meeting Abstracts, OS34A-03.

Paul, J. D., Roberts, G. G., & White, N. (2014). The African landscape through space and time. *Tectonics*, *33*, 898–935. https://doi.org/10.1002/2013TC003479

Peirce, C., Sinha, M., Topping, S., & Gill, C. (2007). Morphology and genesis of slow-spreading ridges–seabed scattering and seismic imaging within the oceanic crust. *Geophysical Journal International*, *168*(1), 59–89.

Purdy, G., Kong, L., Christeson, G., & Solomon, S. (1992). Relationship between spreading rate and the seismic structure of mid-ocean ridges. *Nature*, *355*(6363), 815.

Raitt, M. (1963). The crustal rocks. *The sea*, *3*, 85–102.
Ravelo, A., Andreasen, D. H., Lyle, M., Olivarez Lyle, A., & Wara, M. (2004). Regional climate shifts caused by gradual global cooling in the Pliocene epoch. *Nature*, *429*, 263–267. https://doi.org/10.1038/nature02567
Rohr, K., Milkereit, B., & Yorath, C. (1988). Asymmetric deep crustal structure across the Juan de Fuca Ridge. *Geology*, *16*(6), 533–537.
Ruddiman, W., M. Sarnthein, J. Backman, J. Baldauf, W. Curry, L. Dupont, et al. (1989), *29. Late Miocene to Pleistocene evolution of climate in Africa and the low-altitude Atlantic: Overview of leg 108 results* (Vol. 108, pp. 463–484) https://doi.org/10.2973/odp.proc.sr.108.173.1989.
Ruddiman, W. F., & Janecek, T. R. (1989). Biogenic and terrigeneous components in Pliocene-Pleistocene sediments of the equatorial Atlantic, https://doi.org/10.1594/PANGAEA.746239, supplement to: Ruddiman, WF; Janecek, TR (1989): Pliocene-Pleistocene biogenic and terrigenous fluxes at equatorial Atlantic Sites 662, 663, and 664. In: Ruddiman, W; Sarnthein, M; et al. (eds.), Proceedings of the Ocean Drilling Program, Scientific Results, College Station, TX (Ocean Drilling Program), 108, 211-240, https://doi.org/10.2973/odp.proc.sr.108.165.1989.
Sarnthein, M., Winn, K., Duplessy, J.-C., & Fontugne, M. R. (1988). Global variations of surface ocean productivity in low and mid latitudes: Influence on CO_2 reservoirs of the deep ocean and atmosphere during the last 21,000 years. *Paleoceanography and Paleoclimatology*, *3*(3), 361–399.
Schreiber, E., & Fox, P. J. (1977). Density and *P*-wave velocity of rocks from the FAMOUS region and their implication to the structure of the oceanic crust. *Geological Society of America Bulletin*, *88*(4), 600–608.
Seher, T., Crawford, W. C., Singh, S. C., Cannat, M., Combier, V., & Dusunur, D. (2010). Crustal velocity structure of the lucky strike segment of the Mid-Atlantic Ridge at 37° N from seismic refraction measurements. *Journal of Geophysical Research*, *115*, B03103. https://doi.org/10.1029/2009JB006650
Shaw, P. R. (1994). Age variations of oceanic crust Poisson's ratio: Inversion and a porosity evolution model. *Journal of Geophysical Research*, *99*(B2), 3057–3066.
Sheen, K., White, N., Caulfield, C.-c., & Hobbs, R. (2012). Seismic imaging of a large horizontal vortex at abyssal depths beneath the Aub-Antarctic Front. *Nature Geoscience*, *5*, 542–546. https://doi.org/10.1038/ngeo1502
Shipp, R. M., & Singh, S. C. (2002). Two-dimensional full wavefield inversion of wide-aperture marine seismic streamer data. *Geophysical Journal International*, *151*(2), 325–344.
Singh, S. C., Crawford, W. C., Carton, H., Seher, T., Combier, V., Cannat, M., et al. (2006). Discovery of a magma chamber and faults beneath a Mid-Atlantic Ridge hydrothermal field. *Nature*, *442*(7106), 1029.
Stein, R., H. Ten Haven, R. Littke, J. Rullkotter, and D. Welte (1986). 21. Accumulation of marine and terrigenous organic carbon at upwelling site 658 and nonupwelling sites 657 and 659: Implications for the reconstruction of paleoenvironments in the eastern subtropical Atlantic through Late Cenozoic times1. *In Proceedings of the Ocean Drilling Program: Scientific results* (Vol. 108, p. 361), The Program.
Street-Perrott, F. A., & Perrott, R. A. (1990). Abrupt climate fluctuations in the tropics: The influence of Atlantic Ocean circulation. *Nature*, *343*(6259), 607.
Taylor, M., & Singh, S. (2002). Composition and microstructure of magma bodies from effective medium theory. *Geophysical Journal International*, *149*(1), 15–21.
Tivey, M. A., Johnson, H. P., Fleutelot, C., Hussenoeder, S., Lawrence, R., Waters, C., & Wooding, B. (1998). Direct measurement of magnetic reversal polarity boundaries in a cross-section of oceanic crust. *Geophysical Research Letters*, *25*(19), 3631–3634.
Toomey, D. R., Purdy, G., Solomon, S. C., & Wilcock, W. S. (1990). The three-dimensional seismic velocity structure of the East Pacific Rise near latitude 9°30′ N. *Nature*, *347*(6294), 639.
Van Avendonk, H. J., Shillington, D. J., Holbrook, W. S., & Hornbach, M. J. (2004). Inferring crustal structure in the Aleutian island arc from a sparse wide-angle seismic data set. *Geochemistry, Geophysics, Geosystems*, *5*(8), Q08008. https://doi.org/10.1029/2003GC000664
Vassallo, M., Eggenberger, K., van Manen, D.-J., Özbek, A., & Watterson, P. (2013). Broadband and beyond with marine towed streamers. *The Leading Edge*, *32*(11), 1356–1365.
Vera, E., Mutter, J., Buhl, P., Orcutt, J., Harding, A., Kappus, M., et al. (1990). The structure of 0-to 0.2-my-old oceanic crust at 9° N on the East Pacific Rise from expanded spread profiles. *Journal of Geophysical Research*, *95*(B10), 15,529–15,556.
Vera, E. E., & Diebold, J. B. (1994). Seismic imaging of oceanic layer 2a between 9°30′ N and 10° N on the east pacific rise from two-ship wide-aperture profiles. *Journal of Geophysical Research*, *99*(B2), 3031–3041.
Villinger, H., Grevemeyer, I., Kaul, N., Hauschild, J., & Pfender, M. (2002). Hydrothermal heat flux through aged oceanic crust: Where does the heat escape? *Earth and Planetary Science Letters*, *202*(1), 159–170.
Wagner, T. (2000). Control of organic carbon accumulation in the Late Quaternary Equatorial Atlantic (ocean drilling program sites 664 and 663): Productivity versus terrigenous supply. *Paleoceanography and Paleoclimatology*, *15*(2), 181–199.
Walsh, J. (1988), How much shelf production reaches the deep sea.
White, R. S., McKenzie, D., & O'Nions, R. K. (1992). Oceanic crustal thickness from seismic measurements and rare earth element inversions. *Journal of Geophysical Research*, *97*(B13), 19,683–19,715.
Whitmarsh, R. (1978). Seismic refraction studies of the upper igneous crust in the North Atlantic and porosity estimates for layer 2. *Earth and Planetary Science Letters*, *37*(3), 451–464.
Whittaker, J. M., Goncharov, A., Williams, S. E., Müller, R. D., & Leitchenkov, G. (2013). Global sediment thickness data set updated for the Australian-Antarctic Southern Ocean. *Geochemistry, Geophysics, Geosystems*, *14*, 3297–3305. https://doi.org/10.1002/ggge.20181
Wilkens, R. H., Fryer, G. J., & Karsten, J. (1991). Evolution of porosity and seismic structure of upper oceanic crust: Importance of aspect ratios. *Journal of Geophysical Research*, *96*(B11), 17,981–17,995.
Zhang, Z., Ramstein, G., Schuster, M., Li, C., Contoux, C., & Yan, Q. (2014). Aridification of the sahara desert caused by tethys sea shrinkage during the late miocene. *Nature*, *513*(7518), 401.